

# Exosome-Mediated Crosstalk between Keratinocytes and Macrophages in Cutaneous Wound Healing

Xiaoju Zhou, Brooke A. Brown, Amanda P. Siegel, Mohamed S. El Masry, Xuyao Zeng, Woran Song, Amitava Das, Puneet Khandelwal, Andrew Clark, Kanhaiya Singh, Poornachander R. Guda, Mahadeo Gorain, Lava Timsina, Yi Xuan, Stephen C. Jacobson, Milos V. Novotny, Sashwati Roy, Mangilal Agarwal, Robert J. Lee, Chandan K. Sen, David E. Clemmer,\* and Subhadip Ghatak\*

Cite This: *ACS Nano* 2020, 14, 12732–12748

Read Online

ACCESS |

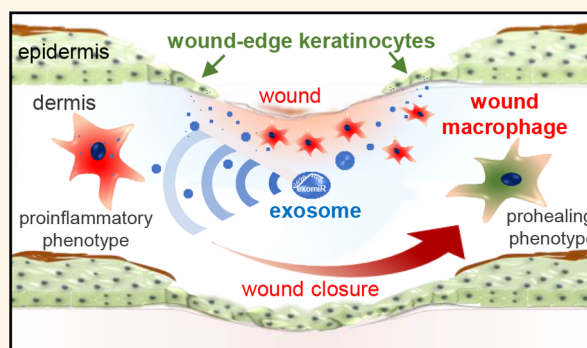
Metrics & More

Article Recommendations

Supporting Information

**ABSTRACT:** Bidirectional cell–cell communication involving exosome-borne cargo such as miRNA has emerged as a critical mechanism for wound healing. Unlike other shedding vesicles, exosomes selectively package miRNA by SUMOylation of heterogeneous nuclear ribonucleoproteinA2B1 (hnRNPA2B1). In this work, we elucidate the significance of exosome in keratinocyte–macrophage crosstalk following injury. Keratinocyte-derived exosomes were genetically labeled with GFP-reporter (Exo<sub>K-GFP</sub>) using tissue nanotransfection (TNT), and they were isolated from dorsal murine skin and wound-edge tissue by affinity selection using magnetic beads. Surface N-glycans of Exo<sub>K-GFP</sub> were also characterized. Unlike skin exosome, wound-edge Exo<sub>K-GFP</sub> demonstrated characteristic N-glycan ions with abundance of low-base-pair RNA and was selectively engulfed by wound macrophages ( $\omega m\phi$ ) in granulation tissue. *In vitro* addition of wound-edge Exo<sub>K-GFP</sub> to proinflammatory  $\omega m\phi$  resulted in conversion to a proresolution phenotype. To selectively inhibit miRNA packaging within Exo<sub>K-GFP</sub> *in vivo*, pH-responsive keratinocyte-targeted siRNA-hnRNPA2B1 functionalized lipid nanoparticles (TLNP<sub>K</sub>) were designed with 94.3% encapsulation efficiency. Application of TLNP<sub>K/si-hnRNPA2B1</sub> to the murine dorsal wound-edge significantly inhibited expression of hnRNPA2B1 by 80% in epidermis compared to the TLNP<sub>K/si-control</sub> group. Although no significant difference in wound closure or re-epithelialization was observed, the TLNP<sub>K/si-hnRNPA2B1</sub> treated group showed a significant increase in  $\omega m\phi$  displaying proinflammatory markers in the granulation tissue at day 10 post-wounding compared to the TLNP<sub>K/si-control</sub> group. Furthermore, TLNP<sub>K/si-hnRNPA2B1</sub> treated mice showed impaired barrier function with diminished expression of epithelial junctional proteins, lending credence to the notion that unresolved inflammation results in leaky skin. This work provides insight wherein Exo<sub>K-GFP</sub> is recognized as a major contributor that regulates macrophage trafficking and epithelial barrier properties postinjury.

**KEYWORDS:** exosome, tissue nanotransfection, keratinocyte-targeted lipid nanoparticles, macrophage, wound healing



The dynamic cellular events following cutaneous injury rely on bidirectional cell–cell communication for efficient wound healing. Such crosstalk is traditionally known to occur via paracrine effects.<sup>1,2</sup> A recent paradigm has emerged wherein the predominant mechanism of cellular communication is attributable to extracellular vesicles (EVs).<sup>3–7</sup> These EVs have distinct structural and biochemical properties depending on their intracellular site of origin that affects their biological function.<sup>8</sup> A majority of these vesicles having diameters ranging from 50 to 1000 nm that originate from the plasma membrane and are often referred to as

microvesicles, ectosomes, microparticles, and exovesicles.<sup>8</sup> Exosomes are a major class of EVs (typically 30–150 nm in diameter) of endocytic origin released by all cell types following

Received: April 11, 2020

Accepted: September 15, 2020

Published: September 15, 2020



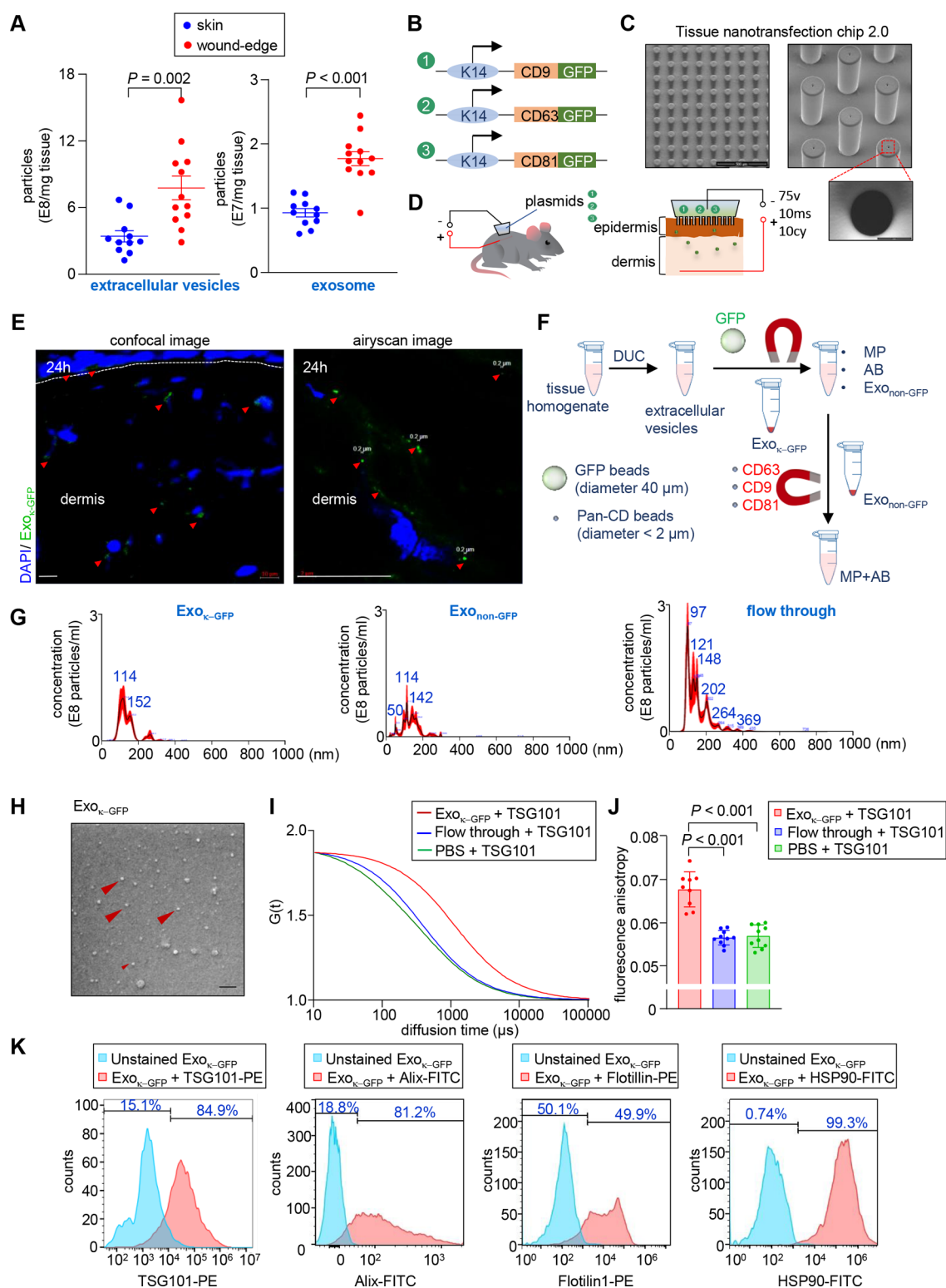


**Figure 1.** Isolation and characterization of keratinocyte-derived exosomes from murine skin. (A) Quantification of extracellular vesicles and exosomes from murine skin and day 5 wound-edge tissue of C57BL/6 mice ( $n = 11, 12$ ). (B) Schematic diagram of keratin 14 (K14) promoter-driven recombinant plasmids encoding CD9, CD63, or CD81 with “in frame” GFP-reporter. (C) Representative scanning electron microscopic images of tissue nanotransfection (TNT) chip 2.0. (D) Schematic diagram showing the delivery of the three K14 promoter-driven plasmids via TNT in the dorsal murine skin. (E) Confocal microscopic images showing the presence of keratinocyte-derived exosome ( $\text{Exo}_{\text{K-GFP}}$ ) in dermis (left) and super-resolution airyscan images showing GFP-labeled exosome (right). The white dashed line shows the epidermal–dermal junction. Scale, 10 and 2  $\mu\text{m}$ . (F) Schematic diagram showing the exosome isolation process from murine skin tissue post-TNT with the three plasmids. DUC, differential ultracentrifugation; MP, membrane particles; AB, apoptotic bodies. (G) Particle size distribution of keratinocyte-derived exosomes ( $\text{Exo}_{\text{K-GFP}}$ ), non-keratinocyte-derived exosomes ( $\text{Exo}_{\text{non-GFP}}$ ), and flow through (membrane particles and apoptotic bodies) from murine skin ( $n = 10$ ). (H) Representative scanning electron microscopy (SEM) images of murine-keratinocyte-derived exosomes. Scale, 100 nm. (I, J) Binding of TSG-101 PE with the murine-keratinocyte-derived exosome was further tested

Figure 1. continued

by autocorrelation curves as determined by fluorescence correlation spectroscopy (FCS) (I) and time-resolved fluorescence anisotropy (J) ( $n = 10$ ). (K) Flow cytometric analysis of murine skin-keratinocyte-derived exosome on GFP-trap magnetic beads showing binding of TSG-101 PE, Alix-FITC, Flotillin 1-PE, and HSP90-FITC antibodies. The histograms demonstrate the shift in fluorescence after binding of murine Exo<sub>K-GFP</sub> on the GFP-trap magnetic beads with the respective antibody. All data were shown as mean  $\pm$  SEM. Data in part A were analyzed by a two-tailed unpaired Student's *t* test. Data in part J were analyzed by one-way ANOVA with the *post hoc* Bonferroni multiple comparison test.

fusion of multivesicular bodies (MVBs) with the plasma membrane.<sup>9,10</sup> Exosomes carry a distinctive repertoire of cargo such as miRNAs.<sup>11</sup> RNA profiling of exosomes showed differences in miRNA abundance compared to the parent cells, suggesting that parent cells possess a sorting mechanism that guides specific intracellular miRNAs to enter into the exosomes.<sup>12–14</sup> SUMOylation of heterogeneous nuclear ribonucleoprotein A2B1 (hnRNPA2B1) has been implicated as a predominant mechanism of miRNA packaging within exosomes.<sup>15</sup> Within the cell, miRNAs have specific sequence motifs that control their localization into exosomes. Binding of hnRNPA2B1 to the miRNA by recognition of these motifs controls their loading into exosomes. Moreover, SUMOylation of hnRNPA2B1 regulates the binding of hnRNPA2B1 to miRNAs. Given the presence of such a well-coordinated sorting mechanism, it is apparent that cell–cell crosstalk via exosomes is an active process. Such a process is distinct from cellular communication mediated via shedding of other membrane vesicles that also carry biomolecules such as miRNA as cargo that is not selectively packaged in these vesicles. Lack of efficient isolation techniques of exosomes from other membrane vesicles of similar size has led to conclusions that are primarily derived from a heterogeneous EV pool. This lack of discrimination among various membrane vesicles dampens the potential significance of exosomes in cellular communication and has impaired discovery of the role of exosome of specific cellular origins in communication.

The putative role of keratinocytes in wound healing and inflammation is well documented.<sup>16–19</sup> At the wound site, cells of myeloid origin such as monocytes and macrophages are primarily responsible for mounting an early inflammatory response to injury.<sup>20–23</sup> Both robust mounting of inflammation as well as timely resolution are key to successful tissue repair. The role of keratinocytes for the resolution of inflammation remains unclear and debated. This study rests on our observation that, at the site of injury, EVs of keratinocyte origin are critical for conversion of the myeloid cells into fibroblast-like cells in the granulation tissue.<sup>19</sup> The objectives of this work were to isolate exosomes of keratinocyte origin at the wound-edge and to delineate their significance in the resolution of inflammation at the wound site. This work shows that keratinocyte-derived exosomes carry miRNAs that direct resolution of macrophage numbers and function within the granulation tissue and are critical for functional wound closure.

## RESULTS AND DISCUSSION

**Identification and Isolation of Keratinocyte-Derived Exosomes in Murine Skin.** To circumvent the EV complexity found *in vivo* in complex tissues, we employed an *in vitro* system and isolated exosomes from the heterogeneous pool of EVs derived from cultured keratinocytes. According to EVPedia<sup>24</sup> and Exocarta,<sup>25</sup> the three tetraspanins CD9, CD63, and CD81 are reliable markers of exosomes.<sup>26</sup> In the interest of rigor, we employed a two-step process to isolate pure exosome. First, EVs were isolated from keratinocyte-conditioned media using

differential ultracentrifugation (Figure S1A). Second, the heterogeneous EVs were incubated with superparamagnetic Dynabeads conjugated with antibodies for CD9, CD63, and CD81 (Figure S1A). From the heterogeneous EV mixture, only the tetraspanins expressing exosomes were trapped, leaving the membrane particles and apoptotic bodies in the flow through. We tested all nine criteria set forward by EV-track for transparent reporting (Figure S1). The size and concentration of the exosomes were analyzed by nanoparticle tracking analysis (NanoSight) and scanning electron microscopy (SEM) (Figure S1B,C). The density of the isolated exosomes was found to be 1.16 g/mL. The isolated exosomes showed an abundance of other reported exosome markers such as Alix, TSG101, HSP90, and Flotillin 1 (Figure S1D). The purity of the isolation was tested by immunoblotting of GM130 and Prohibitin that are reported as major contaminants of exosome preparation by EV-track.<sup>27</sup> Additional quantitative analysis such as flow cytometry of these Dynabeads post-adsorption with exosomes following incubation with phycoerythrin (PE) conjugated TSG101 (TSG101-PE) antibody showed an increased shift in fluorescence intensity (Figure S1E). Furthermore, binding of PE tagged TSG101 antibody was tested by fluorescence anisotropy (Figure S1F) and fluorescence correlation spectroscopy (Figure S1G). Binding of TSG101-PE by the resuspended isolated exosomes hindered their free rotation, as shown by a marked increase in fluorescence anisotropy (Figure S1F). TSG101-PE had fast and unhindered diffusion when resuspended in PBS or in the presence of EV flow through. However, in the presence of exosomes, diffusion of TSG101-PE slowed down, as shown by the shifted autocorrelation curve (Figure S1G). These data validated that the two-step isolation process was successful in separating exosomes from the heterogeneous EV pool. This method of exosome isolation was reported in EV-track (EV190103) with a preliminary EV-METRIC of 100%.<sup>28</sup>

The approach described above was applied for isolation of exosomes *in vivo*. Recent reports have highlighted the role of exosome in cutaneous wound healing.<sup>29,30</sup> Analysis of EV concentration from murine skin and day 5 wound-edge tissue (<2 mm from the wound-edge) showed a significant increase in EVs as well as exosomes in day 5 wound-edge tissue (Figure 1A). Quantitative analysis revealed that exosomes represent only about 10% of the total EV pools. In addition to the resident cells such as keratinocytes and fibroblasts, day 5 wound-edge tissue contains infiltrated blood-borne cells including macrophages. Thus, to understand whether the increased abundance of exosomes at the wound edge is due to increased release of exosomes by additional biogenesis in resident cells or contributed by infiltrating cells, it becomes critical to segregate the exosomes based on their cellular origin.

Our previous work has recognized the critical role of keratinocyte-derived EV in the conversion of injury-site myeloid cells to fibroblast-like cells in granulation tissue.<sup>19</sup> However, the significance of exosomes in such keratinocyte–myeloid cell crosstalk remains unknown. Since one or more of the three tetraspanins CD9, CD63, and CD81 are expressed in all

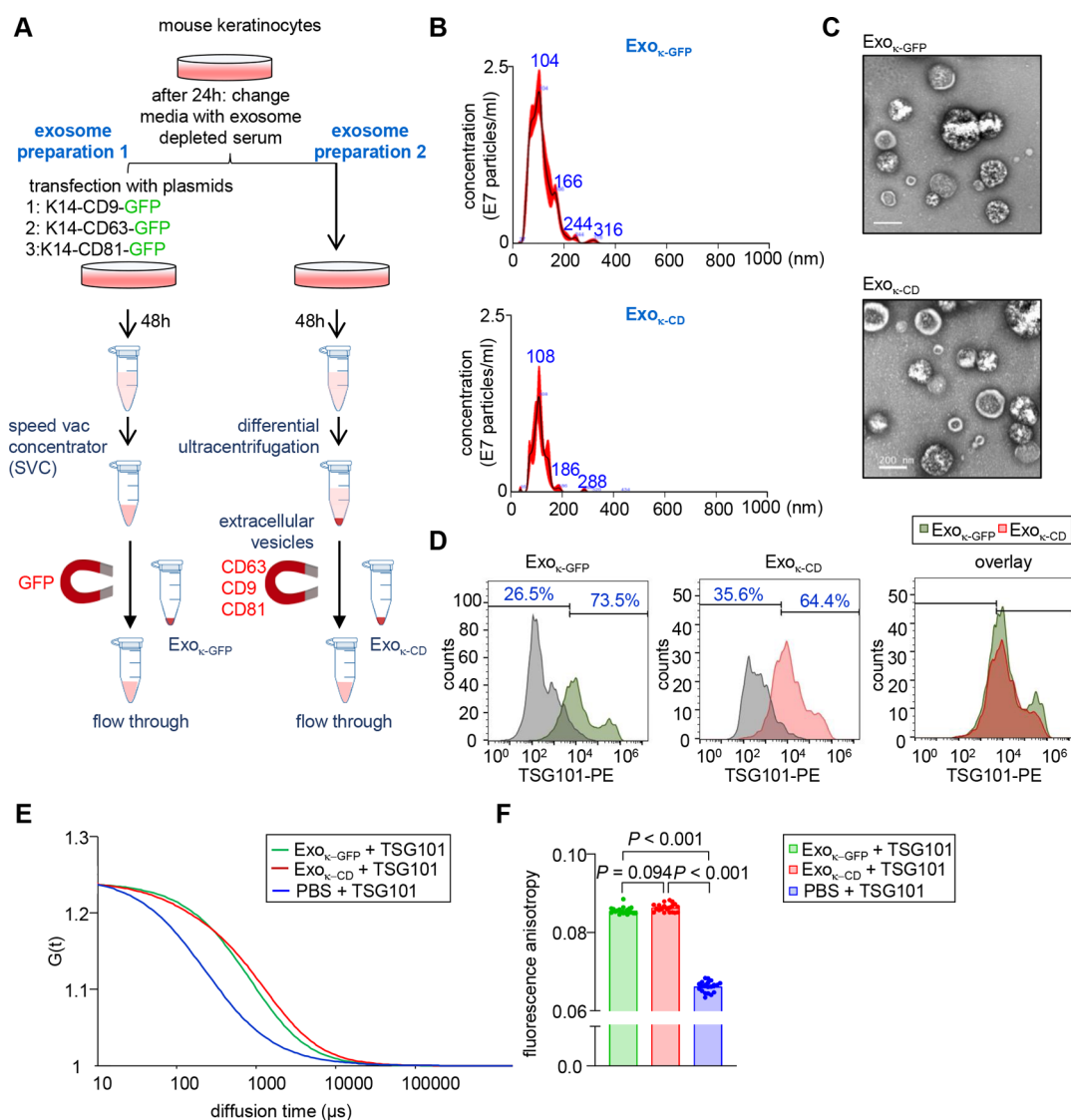


**Figure 2.** Comparative analysis of keratinocyte-derived exosome with exosome isolated from cell culture conditioned media. (A) Schematic diagram showing the exosome isolation process from murine keratinocyte (Kera308) cultured media with and without transfection with keratin 14 promoter-driven recombinant plasmids encoding CD9, CD63, or CD81 with “in frame” GFP-reporter. (B) The particle size distribution of exosomes and eluent (membrane particles and apoptotic bodies) from murine keratinocyte cultured media ( $n = 6$ ). (C) Representative transmission electron microscopy (TEM) images of exosomes isolated using GFP beads and CD beads. Scale, 200 nm. (D) Flow cytometric analysis of murine-keratinocyte-derived exosome on CD magnetic beads (CD63, CD9, and CD81) and GFP beads showing binding of TSG-101 PE antibody. (E, F) Binding of TSG-101 PE with the murine-keratinocyte-derived exosome was further tested by autocorrelation curves, as determined by fluorescence correlation spectroscopy (FCS) (E) and time-resolved fluorescence anisotropy (F) ( $n = 20$ ). All data were shown as mean  $\pm$  SEM. Data in part F were analyzed by one-way ANOVA with the *post hoc* Bonferroni multiple comparison test.

exosomes, we designed three murine keratin 14 (K14) promoter-driven plasmids that encode for CD9, CD63, and CD81 with “in frame” GFP-reporter (Figure 1B). Such promoter-driven plasmids allow expression of GFP-tagged CD markers only in keratinocytes. The specificity of the plasmid cocktail was tested in murine keratinocytes, fibroblasts, and *ωmφ* (Figure S2A–C). We tested the hypothesis that *in vivo* topical delivery of these three plasmids would result in the expression of GFP in all exosomes that are of keratinocyte origin. We have previously reported that cutaneous delivery of reprogramming molecules via tissue nanotransfection (TNT) was efficient and effective in directly reprogramming dermal fibroblast cells into a variety of functionally distinct lineages.<sup>31</sup> We have now generated a modified TNT silicon chip (TNT<sub>2.0</sub>) with a longer needle height of 170  $\mu\text{m}$  and a pore diameter of 4

$\mu\text{m}$  (Figure 1C). Modifying the electrical potential applied between the cargo within the chip and skin led to stepwise increases in the depth of transfection of fluorescein amidite (FAM)-labeled DNA (Figure 1D, Figure S2D) in wild type C57BL/6 mice. Delivery of these three K14 promoter-driven plasmids via TNT followed by super-resolution confocal microscopy demonstrated the presence of exosomes with GFP-reporter expression in the epidermis as well as in the dermis (Figure 1E, Figure S2E). Because the GFP-reporter protein was cloned in frame with the CD9, CD63, and CD81, pull down of GFP using magnetic traps is expected to isolate the Exo<sub>K-GFP</sub>. Keratinocyte-derived exosomes were isolated from the tissue homogenate using GFP-magnetic traps followed by separating the exosomes from the beads using elution buffer (Figure 1F). The resultant flow through was further ultra-

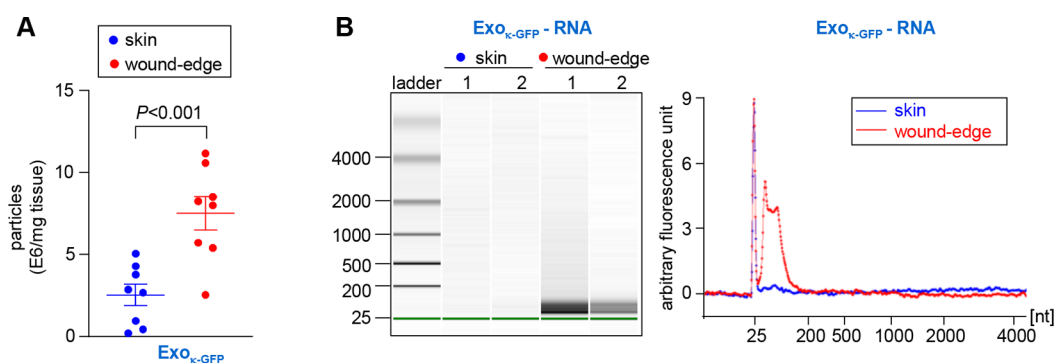


**Figure 3.** Characterization of keratinocyte-derived exosome from murine skin and wound-edge tissue. (A) Murine dorsal skin was transfected with keratin 14 promoter-driven recombinant plasmids encoding CD9, CD63, or CD81 with “in frame” GFP-reporter via TNT. The keratinocyte-derived exosomes were isolated from skin and day 5 wound-edge tissue using a GFP-magnetic trap and quantified using NTA. Data were shown as mean  $\pm$  SEM and were analyzed by two-tailed unpaired Student’s *t* test ( $n = 8$ ). (B) High-resolution automated electrophoresis of RNA isolated from skin and wound-edge Exo<sub>K-GFP</sub>. RNA in wound-edge Exo<sub>K-GFP</sub> was significantly abundant compared to that of skin Exo<sub>K-GFP</sub>.

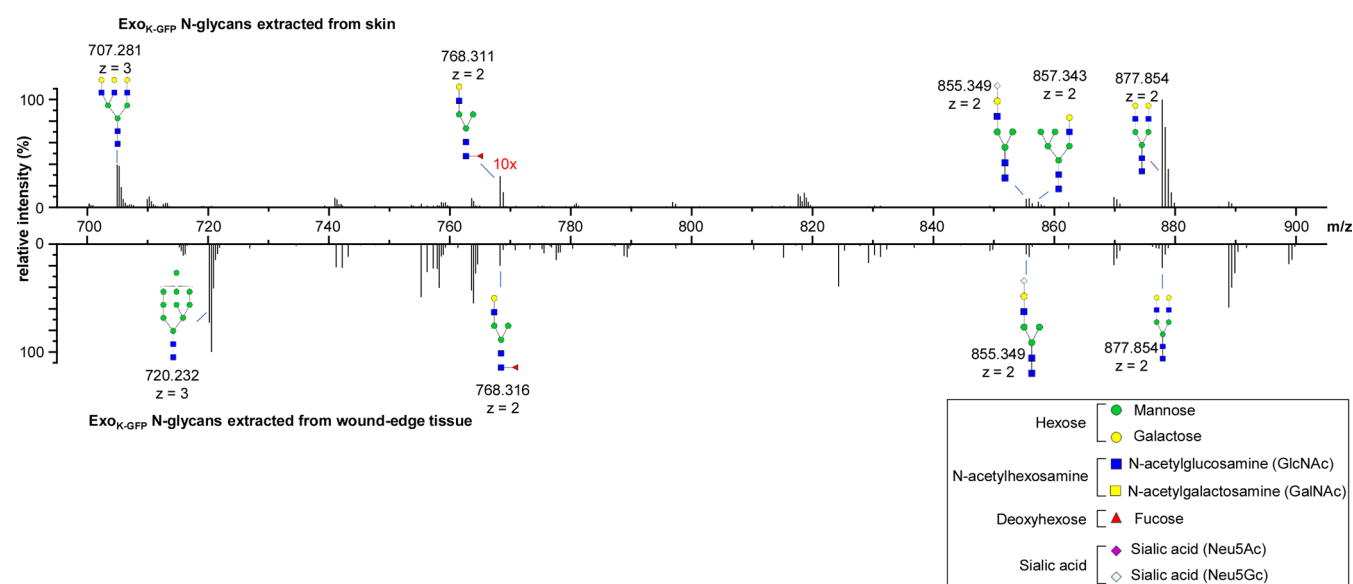


**Figure 4.** Comparative glycomics of the Exo<sub>K-GFP</sub> isolated from skin and wound-edge tissue. Representative  $m/z$  ratios, relative intensities, and proposed structures of N-glycans released from skin- and wound-edge-tissue-derived Exo<sub>K-GFP</sub>, methylamidated, labeled with Girard’s reagent T, and analyzed by CE-MS. Data analysis determined that 19 and 7 structures were found exclusive to skin and day 5 wound-edge tissue, respectively.

centrifuged, and the non-keratinocyte-derived exosomes (Exo<sub>non-GFP</sub>) were isolated using pan-CD superparamagnetic beads (Figure 1F). The size and concentration of Exo<sub>K-GFP</sub> and Exo<sub>non-GFP</sub> and flow through were further examined using nanoparticle tracking analysis (Nanosight) (Figure 1G). Scanning electron microscopy of Exo<sub>K-GFP</sub> revealed the presence of exosomes of different size (Figure 1H). Adsorption of Exo<sub>K-GFP</sub> on GFP-trap was tested by fluorescence correlation spectroscopy (Figure 1I) and fluorescence anisotropy (Figure 1J). Flow cytometric analysis of GFP-trap beads post-adsorption with Exo<sub>K-GFP</sub> following incubation with fluorescently tagged antibodies of exosome markers such as TSG101-PE, Alix-FITC, Flotilin1-PE, and HSP90-FITC showed an increase in fluorescence intensity (Figure 1K). These findings demonstrate that the GFP-trap approach was successful in isolating Exo<sub>K-GFP</sub> from murine tissue homogenate.

Ultracentrifugation is widely held as a gold standard for exosome isolation. In the interest of rigor, Exo<sub>K-GFP</sub> was subjected to direct comparison with exosomes isolated using

differential ultracentrifugation. Murine keratinocytes were transfected with the three K14 promoter-driven plasmids to label the exosomes with GFP-reporter. Exosomes were isolated from the cell culture supernatant using GFP-trap and compared with exosomes isolated using ultracentrifugation (Figure 2A). No differences in size, shape, and binding property were observed between the exosomes isolated using the two methodologies (Figure 2B–F).

#### Characterization of Keratinocyte-Derived Exosomes Isolated from Murine Skin and Wound-Edge Tissue.

Isolation of Exo<sub>K-GFP</sub> from wild type mice showed a significant increase in day 5 wound-edge Exo<sub>K-GFP</sub> compared to skin (Figure 3A). High-resolution automated electrophoresis of RNA isolated from Exo<sub>K-GFP</sub> showed an abundance of small bp RNA (<100 bp) in day 5 wound-edge tissue (Figure 3B). These data suggest Exo<sub>K</sub>-borne miRNA signals are dispatched from resident keratinocytes of the wound-edge tissue to enable crosstalk with visiting immune cells.

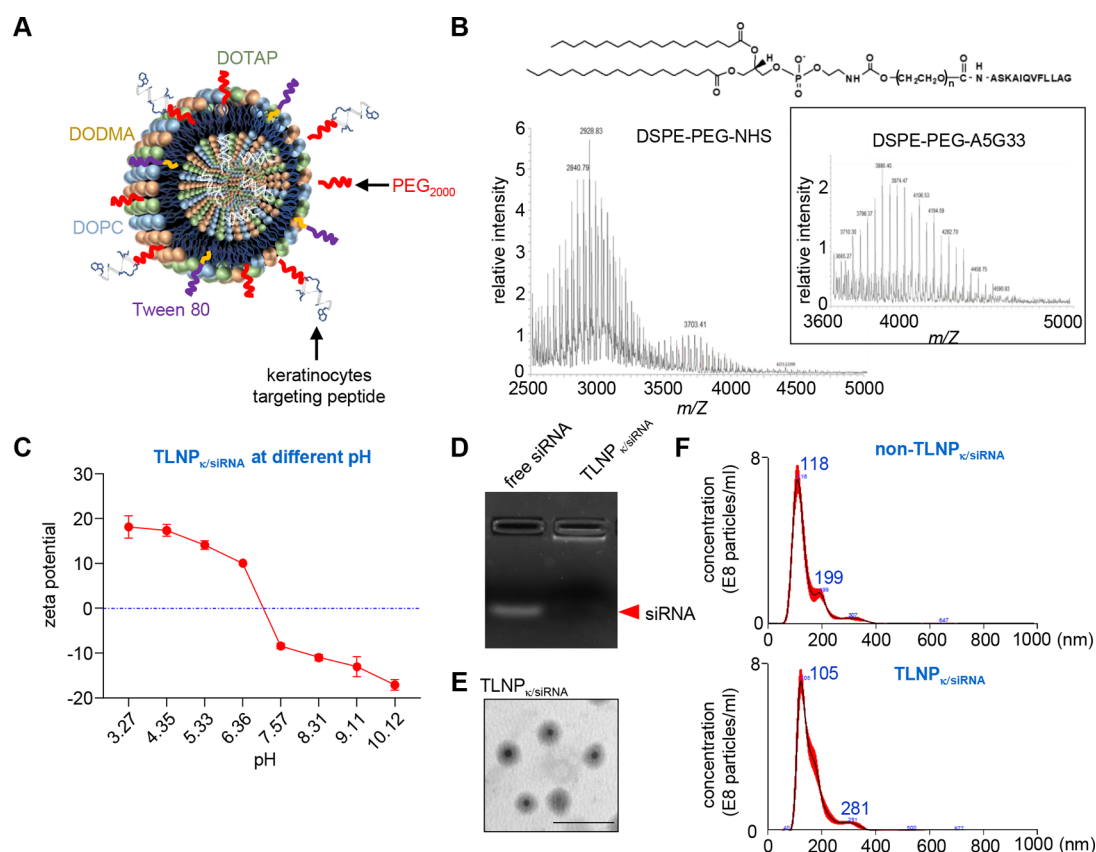


**Figure 5.** Design and synthesis of keratinocyte-targeted lipid nanoparticles (TLNP $_{\kappa}$ ) to inhibit miRNA packaging within exosome. (A) Schematic representation of the keratinocyte-targeted lipid nanoparticles TLNP $_{\kappa}$ . (B) Mass spectrometric analysis of DSPEPEG 2000-A5G33 and DSPE-PEG-NHS using MALDI-TOF. (C) Zeta potentials of TLNP $_{\kappa}$  at different pH values. (D) Gel retardation assay of TLNP $_{\kappa}$  showing the encapsulation efficiency of TLNP $_{\kappa}$ . (E) Representative transmission electron microscopy (TEM) image of TLNP $_{\kappa}$ . Scale, 500 nm. (F) Representative nanoparticle tracking analysis (NanoSight) showing the particle size distribution and concentration of non-TLNP $_{\kappa}$  and TLNP $_{\kappa}$ .

**N-Glycan Molecules Facilitate the Uptake of Keratinocyte-Derived Exosomes by the Macrophage at the Wound Edge.** Based on our previous work that demonstrated the critical role of EVs of keratinocyte origin in the conversion of injury-site myeloid cells to fibroblast-like cells of granulation tissue,<sup>19</sup> it is plausible that the exosomes released from the keratinocytes are likely engulfed by the  $\omega\text{m}\phi$ . Immunohistochemistry followed by super-resolution confocal microscopic images revealed that, unlike the skin adjacent to the wound, the Exo $_{\kappa\text{-GFP}}$  at the wound edge were selectively engulfed by the  $\omega\text{m}\phi$  (Figure S3A–C). Macrophage has abundant membrane-bound C-type lectin receptors that share a common carbohydrate recognition domain.<sup>32</sup> Such receptors are critical for binding to specific carbohydrate structures of endogenous self-molecules.<sup>33</sup> The C-type lectin receptors on a macrophage membrane are able to bind branched sugars with terminal mannose, fucose, or N-acetyl-glucosamine and mediate both endocytosis and phagocytosis.<sup>34</sup> Intrigued by the site-specific selective uptake of Exo $_{\kappa\text{-GFP}}$  by the  $\omega\text{m}\phi$ , we tested the hypothesis that, at the wound edge, the Exo $_{\kappa\text{-GFP}}$  surface is selectively modified to facilitate uptake by the immune cells. Exo $_{\kappa\text{-GFP}}$  N-glycans were analyzed by capillary electrophoresis-mass spectrometry (CE-MS) to identify N-glycan compositions.<sup>35,36</sup> Released, purified, and methylamidated N-glycans were labeled with Girard's reagent T (GT) to impart a single positive charge for electrophoretic separation and enhanced ionization efficiency during CE-MS analysis. The compositions and tentative structures of the glycans were based on detected

mass and the ExpASY GlyConnect database.<sup>37</sup> Through CE-MS, 51 N-glycan compositions were identified in total (Table S1), among which 19 and 7 glycans were exclusively present in skin and day 5 wound-edge tissue, respectively. Furthermore, N-glycans conserved in both skin and day 5 wound edge differ in their relative intensities (Figure 4). Glycans with  $m/z$  855.349 (corresponding to Hex<sub>4</sub>HexNAc<sub>3</sub>Neu5Gc<sub>1</sub>) existed in both Exo $_{\kappa\text{-GFP}}$  samples with similar relative intensities. However, glycan ions at  $m/z$  877.8542 (Hex<sub>5</sub>HexNAc<sub>4</sub>) were more abundant in skin Exo $_{\kappa\text{-GFP}}$ , whereas glycan ions at  $m/z$  707.281 (Hex<sub>6</sub>HexNAc<sub>5</sub>) were found exclusively in skin Exo $_{\kappa\text{-GFP}}$ . Similarly, glycan ions at  $m/z$  720.232 (Hex<sub>10</sub>HexNAc<sub>2</sub>) were only detected in wound-edge Exo $_{\kappa\text{-GFP}}$ . The difference in the abundance of glycan molecules on the Exo $_{\kappa\text{-GFP}}$  surface lends credence to the notion that they play a role in uptake by  $\omega\text{m}\phi$  during wound healing. *In vitro* inhibition of the C-type lectin receptors in day 3  $\omega\text{m}\phi$  resulted in decreased uptake of Exo $_{\kappa\text{-GFP}}$  (Figure S3C,D and Supporting Movie S3 and S4). It was thus of interest to test whether Exo $_{\kappa\text{-GFP}}$  determines the fate of myeloid cells at the wound site. The conventional M1/M2 nomenclature is not appropriate for  $\omega\text{m}\phi$ .<sup>23,38,39</sup> Recognizing the ambiguity in macrophage nomenclature specifically for tissue macrophages,<sup>40–42</sup> we classify *in vivo*  $\omega\text{m}\phi$  on the basis of the proinflammatory or proresolution/healing phenotype. Incubation of day 3  $\omega\text{m}\phi$  (proinflammatory phenotype) with Exo $_{\kappa\text{-GFP}}$  and Exo $_{\text{non-GFP}}$  isolated from day 3 wound-edge tissue (Figure S3E) caused overt phenotypic changes. On day 7, down-regulation of proinflammatory genes such as *Tnfa*, *Nos2*, and

Cd74 was associated with upregulation of the proresolution gene *Cl3* (Figure S3F).

**Design and Synthesis of Keratinocyte-Specific Lipid Nanoparticles to Inhibit miRNA Packaging within Exosome.** Exosomes carry a distinctive repertoire of cargo such as miRNAs.<sup>11</sup> Previous studies on RNA profiling of exosomes showed the difference in miRNA abundance compared to the parent cells, suggesting that parent cells possess a sorting mechanism that guides specific intracellular miRNAs to enter into the exosomes.<sup>12–14</sup> Should the cues for conversion of wound macrophage from a proinflammatory to a proresolution state be driven by keratinocytes via miRNA packaged in exosome, then inhibition of such packaging machinery would result in accumulation of proinflammatory macrophage *in vivo*. SUMOylation of heterogeneous nuclear ribonucleoprotein (hnRNPA2B1) has been implicated in miRNA packaging within exosomes.<sup>15</sup> ExomiRs contain a distinct signature motif known as an exomotif. Exomotif are recognized by heterogeneous nuclear ribonucleoprotein (hnRNPA2B1). Exosomal loading of exomiRs is thus controlled by hnRNPA2B1.<sup>15</sup> SUMOylation of hnRNPA2B1 causes a gain in function, thus improving exosomal loading of miRNA. Thus, it is plausible that inhibition of hnRNPA2B1 in the keratinocytes would impair the microRNA packaging in Exo<sub>K</sub>-GFP. We have previously reported keratinocyte-targeted delivery of oligonucleotide using functionalized lipid nanoparticles.<sup>43</sup> Using a similar approach, we designed keratinocyte-targeted siRNA functionalized lipid nanoparticles (TLNP<sub>K</sub>) to inhibit the expression of hnRNPA2B1 in keratinocytes (Figure 5A). Unlike our previous report, the DODAP was replaced by DODMA containing pH-sensitive tertiary amine (Figure 5A). Additionally, the keratinocyte-targeting peptide ASKAIQVFLLAG (A5G33) peptide was conjugated with NHS-PEG<sub>2000</sub>-DSPE in a one-step process for better purification (Figure 5B). A high concentration of Tween 80 (20 mol %) used in nanoparticle formulation for a reduction in the particle size, stabilization of the nanoparticle and increased the skin permeability for local delivery. The zeta potentials ( $\zeta$ ) of TLNP<sub>K</sub> changed from +20 to -20 mV in the pH range of 3–10, demonstrating the pH-sensitive activity of TLNP<sub>K</sub> (Figure 5C). Within the physiological limit, the neutral or mild positive charge of the lipid nanoparticles evades uptake by the reticuloendothelial system (RES), prolong circulation time, and reduce the toxicity.<sup>44–46</sup> The siRNA encapsulation efficiency was found to be more than 90% when measured by the Quant-iT RiboGreen RNA Kit. The gel retardation assay further demonstrated that the siRNA formed complexes with lipid nanoparticles (Figure 5D). The average size of the lipid nanoparticles was found to be 108.9 nm (Figure 5E,F). In a mixed culture comprised of keratinocytes, endothelial cells, and fibroblasts, TLNP<sub>K</sub> was specifically taken up by the keratinocytes within 4 h, demonstrating targeting specificity and efficiency (Figure 6A,B, Figure S4A,B). This TLNP<sub>K</sub> was not cytotoxic in keratinocytes, as determined by LDH release (Figure 6C), metabolic viability (Figure S4C), and propidium iodide exclusion (Figure S4D). The uptake of TLNP<sub>K</sub> by murine keratinocytes was more rapid compared to non-TLNP<sub>K</sub> (Figure 6C, Figure S4E). All materials used for its formulation have prior history of FDA approval for human use and thus offer a clear translational advantage.

**Functional Characterization of Keratinocyte-Specific Lipid Nanoparticles to Inhibit miRNA Packaging within Exosome.** To test whether our siRNA functionalized

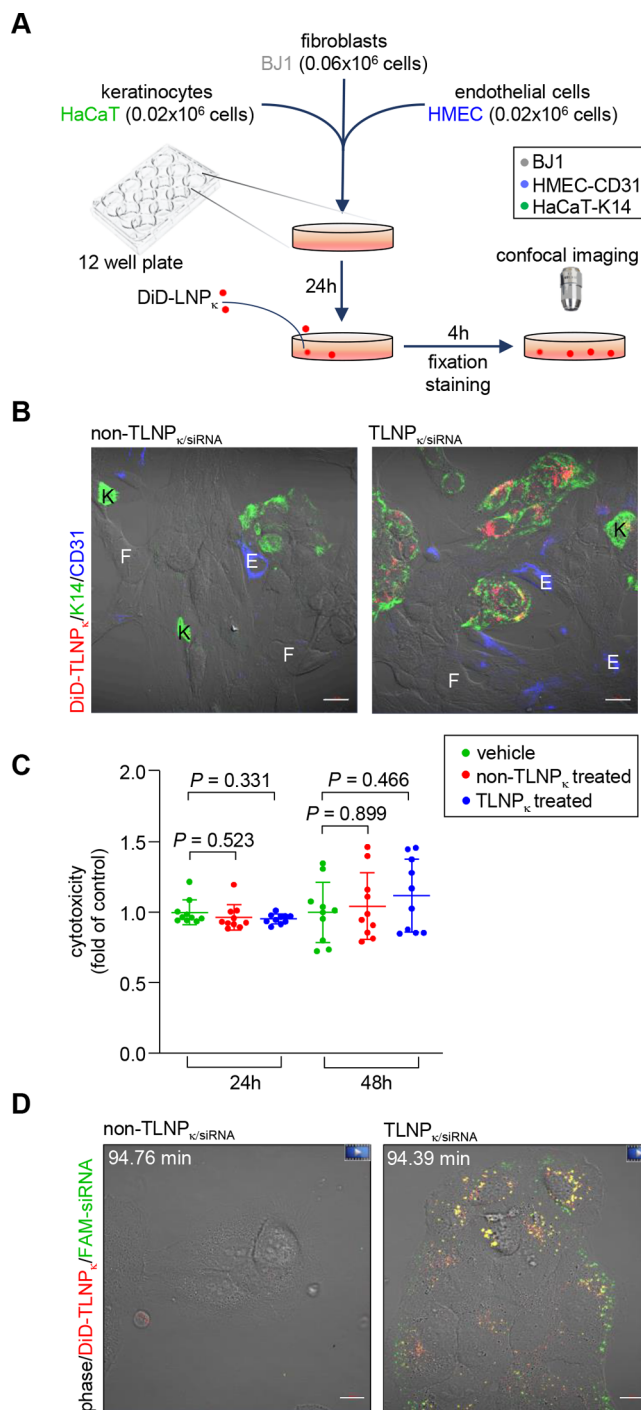


**Figure 6.** Specificity, uptake, and cytotoxicity of keratinocyte-targeted lipid nanoparticles (TLNP<sub>K</sub>). (A) Schematic diagram showing the experimental design to test the specificity of TLNP<sub>K</sub> in mixed culture. (B) Confocal microscopic images showing selective uptake of TLNP<sub>K</sub> by human keratinocytes at 4 h compared with non-TLNP<sub>K</sub> in mixed culture cells (HaCaT:HMEC:BJ-1 = 1:1:3). K, keratinocyte; F, fibroblasts; E, endothelial cells. Scale, 20  $\mu\text{m}$ . (C) *In vitro* LDH assay of TLNP<sub>K</sub> ( $n = 10$ ). (D) Live-cell confocal images showing rapid uptake of TLNP<sub>K</sub> by mouse keratinocytes compared to non-TLNP<sub>K</sub>. Scale, 10  $\mu\text{m}$ .

indicates movies in the Supporting Information. Data in part C were shown as mean  $\pm$  SEM and were analyzed by one-way ANOVA with the *post hoc* Sidak multiple comparison test.

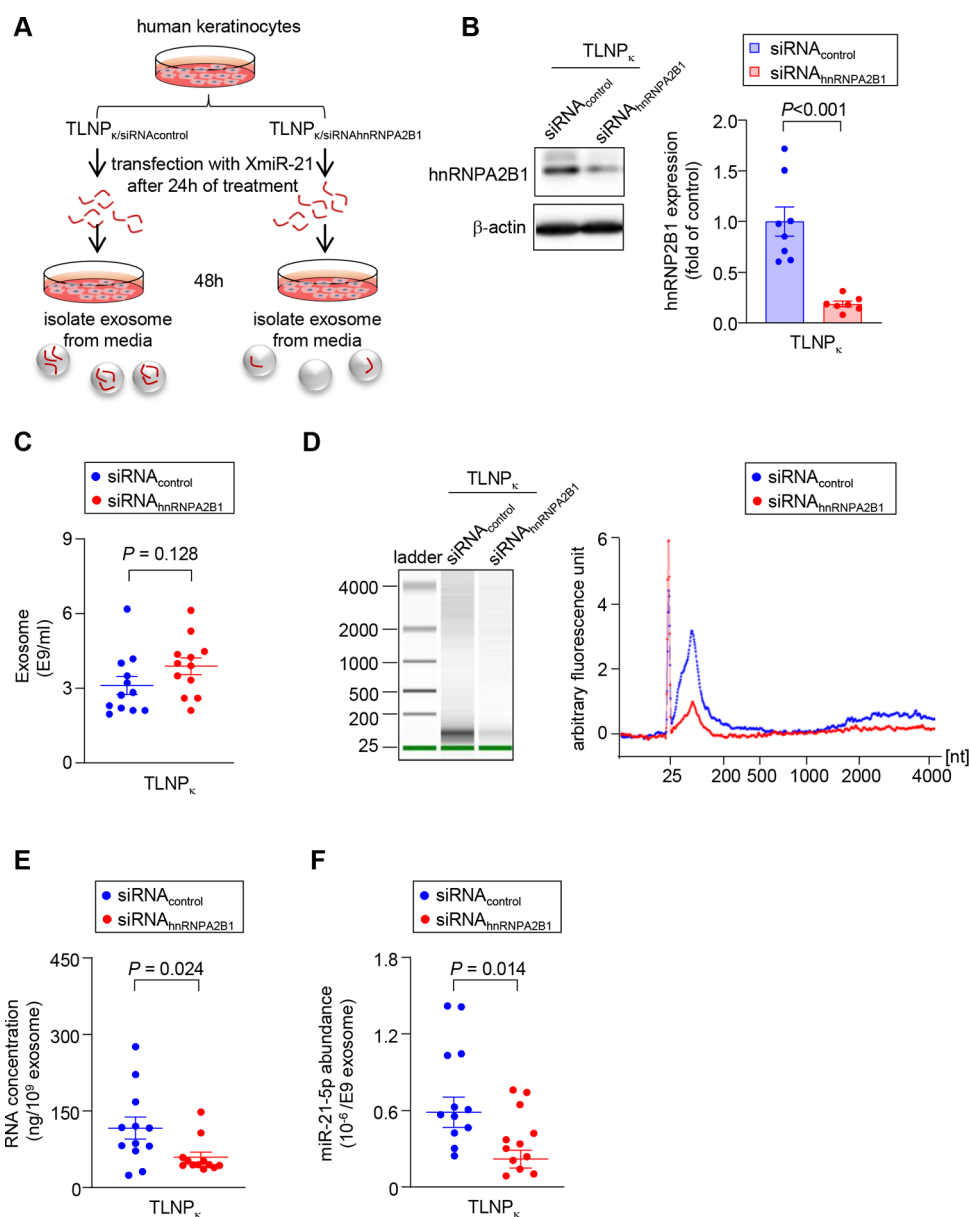


**Figure 7.** TLNP<sub>κ</sub>/si-hnRNP2B1 inhibits packaging of miRNA within the exosome in keratinocyte. (A) Schematic diagram showing the experimental design to test the efficacy of TLNP<sub>κ</sub>/si-hnRNP2B1 in inhibiting miRNA packaging within the exosome in keratinocyte. (B) Western blot analysis of hnRNP2B1 in human keratinocytes 72 h after treatment with TLNP<sub>κ</sub> encapsulating either si-control or si-hnRNP2B1. Quantification of hnRNP2B1 expression from immunoblots ( $n = 8, 7$ ). (C) The exosomes isolated from keratinocyte conditioned media 48 h after transfection and nanoparticle tracking analysis was done. The exosome concentration in the conditioned media 48 h after treatment with TLNP<sub>κ</sub> encapsulating either si-control or si-hnRNP2B1 was plotted graphically ( $n = 12$ ). (D) High-resolution automated electrophoresis of RNA isolated from exosomes in the conditioned media 48 h after treatment with TLNP<sub>κ</sub> encapsulating either si-control or si-hnRNP2B1 was plotted graphically. (E) The RNA concentration per 10<sup>9</sup> exosomes in the conditioned media 48 h after treatment with TLNP<sub>κ</sub> encapsulating either si-control or si-hnRNP2B1 was plotted graphically ( $n = 12$ ). (F) The abundance of miR-21-5p in exosome isolated from the conditioned media 48 h after treatment with TLNP<sub>κ</sub> encapsulating either si-control or si-hnRNP2B1 was plotted graphically ( $n = 12$ ). Data in parts B, C, E, and F were shown as mean  $\pm$  SEM and were analyzed by two-tailed unpaired Student's *t* test.

keratinocyte-targeted lipid nanoparticles are effective in inhibiting the packaging of the miRNA within Exo<sub>κ</sub>-GFP, we utilized commercially available XMIR technology from SBI System Biosciences. XMIR technology takes advantage of normal cellular processes to package a specific miRNA into exosomes using the XMotif RNA sequence tag. Transfection of XmiR-21-5p to human keratinocytes increased the abundance of miR-21-5p in cells as well as in the exosome isolated from keratinocytes cultured conditioned media (Figure 5S,A,B). Delivery of TLNP<sub>κ</sub>/si-hnRNP2B1 to human keratinocyte signifi-

cantly suppressed hnRNP2B1 expression (Figure 7A,B). Transfection of XmiR-21-5p to cells treated with either TLNP<sub>κ</sub>/si-control or TLNP<sub>κ</sub>/si-hnRNP2B1 showed no significant difference in the number of exosomes released by keratinocytes (Figure 7C). However, quantification of exosomal RNA content and miR-21-5p abundance within the exosome from TLNP<sub>κ</sub>/si-hnRNP2B1 and XmiR-21-5p treated keratinocytes showed significant reduction, suggesting that TLNP<sub>κ</sub>/si-hnRNP2B1 was successful in inhibiting the miRNA packaging within the exosome in keratinocytes (Figure 7D–F).

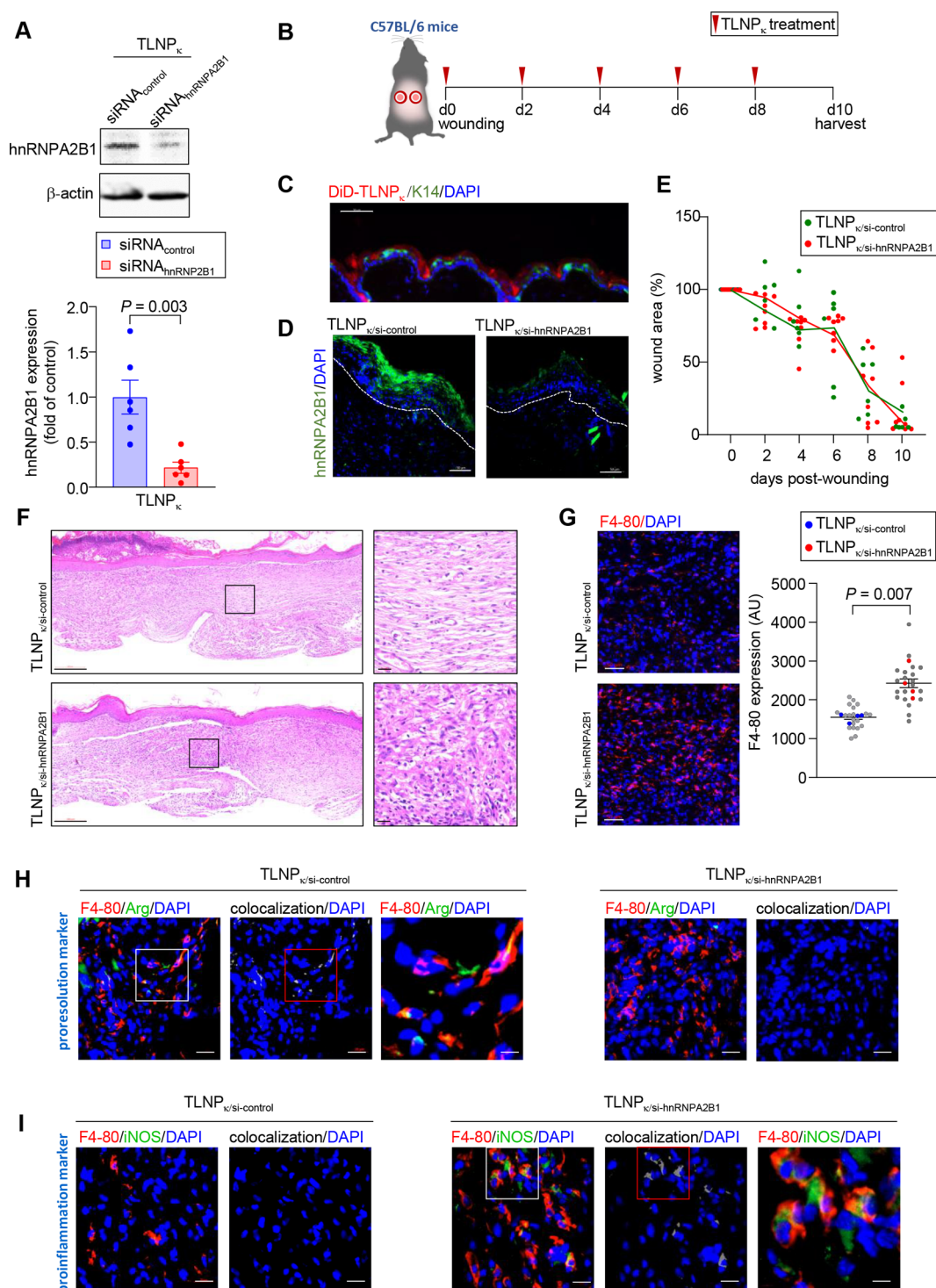


**Figure 8.** Delivery of keratinocyte-targeted lipid nanoparticles encapsulating si-hnRNA2B1 compromised the quality of wound closure. (A) Western blot analysis of hnRNA2B1 in murine keratinocytes 48 h after treatment with TLNP<sub>κ</sub> encapsulating either si-control or si-hnRNA2B1. β-actin was used as a loading control. Quantification of hnRNA2B1 expression from immunoblots ( $n = 6$ ). (B) Schematic diagram showing excisional wounding (6 mm stented wound), application of TLNP<sub>κ</sub> encapsulating either si-control or si-hnRNA2B1, and tissue harvesting time points in C57BL/6 (wild type) mice. (C) Confocal microscopic image showing localization of DID-labeled TLNP<sub>κ</sub> (red) in the epidermis (green) at 24 h after post-treatment with DID-labeled TLNP<sub>κ</sub> by subcutaneous injection. Scale, 50  $\mu\text{m}$ . (D) Representative co-immunofluorescence images showing hnRNA2B1 (green) and DAPI counterstaining in C57BL/6 mice at day 6 post-wounding. White dashed lines indicate the dermal–epidermal junction. Scale, 50  $\mu\text{m}$ . (E) Quantification of excisional stented punch wounds (6 mm) at different days by digital planimetry following delivery of TLNP<sub>κ</sub> encapsulating either si-control or si-hnRNA2B1 ( $n = 6, 8$ ). (F) Representative hematoxylin and eosin (H&E) staining of day 10 murine wound tissue treated with TLNP<sub>κ</sub> encapsulating either si-control or si-hnRNA2B1. Scale, 200  $\mu\text{m}$  (for mosaic images) and 20  $\mu\text{m}$  (for inset images). (G) Representative co-immunofluorescence staining of F4-80 (red) with DAPI counterstaining in wound-edge tissue at day 10 postwounding in C57BL/6 mice treated with either scramble or si-hnRNA2B1 encapsulated keratinocyte-targeted lipid nanoparticles. Scale, 50  $\mu\text{m}$ . Quantification of F4-80 intensity in wound-edge tissue at day 10 postwounding. Each dot

Figure 8. continued

corresponds to one quantified ROI, except the blue and red dots, which correspond to the mean of each mouse. At least 5 ROI per mouse ( $n = 4$ ). (H) Representative co-immunofluorescence staining of F4-80 (red) and arginase (green; proresolution macrophage marker) with DAPI counterstaining in day 10 wound-edge tissue of C57BL/6 mice treated with TLNP $_{\kappa}$  encapsulating either si-control or si-hnRNPA2B1. The colocalization of red and green is shown as white dots. Scale, 20  $\mu\text{m}$ . (I) Representative co-immunofluorescence staining of F4-80 (red) and iNOS (green; proinflammatory macrophage marker) with DAPI counterstaining in day 10 wound-edge tissue of C57BL/6 mice treated with TLNP $_{\kappa}$  encapsulating either si-control or si-hnRNPA2B1. The colocalization of red and green is shown as white dots. Scale, 20  $\mu\text{m}$ . Data in parts A, G, and E were shown as mean  $\pm$  SEM and were analyzed by two-tailed unpaired Student's  $t$  test.

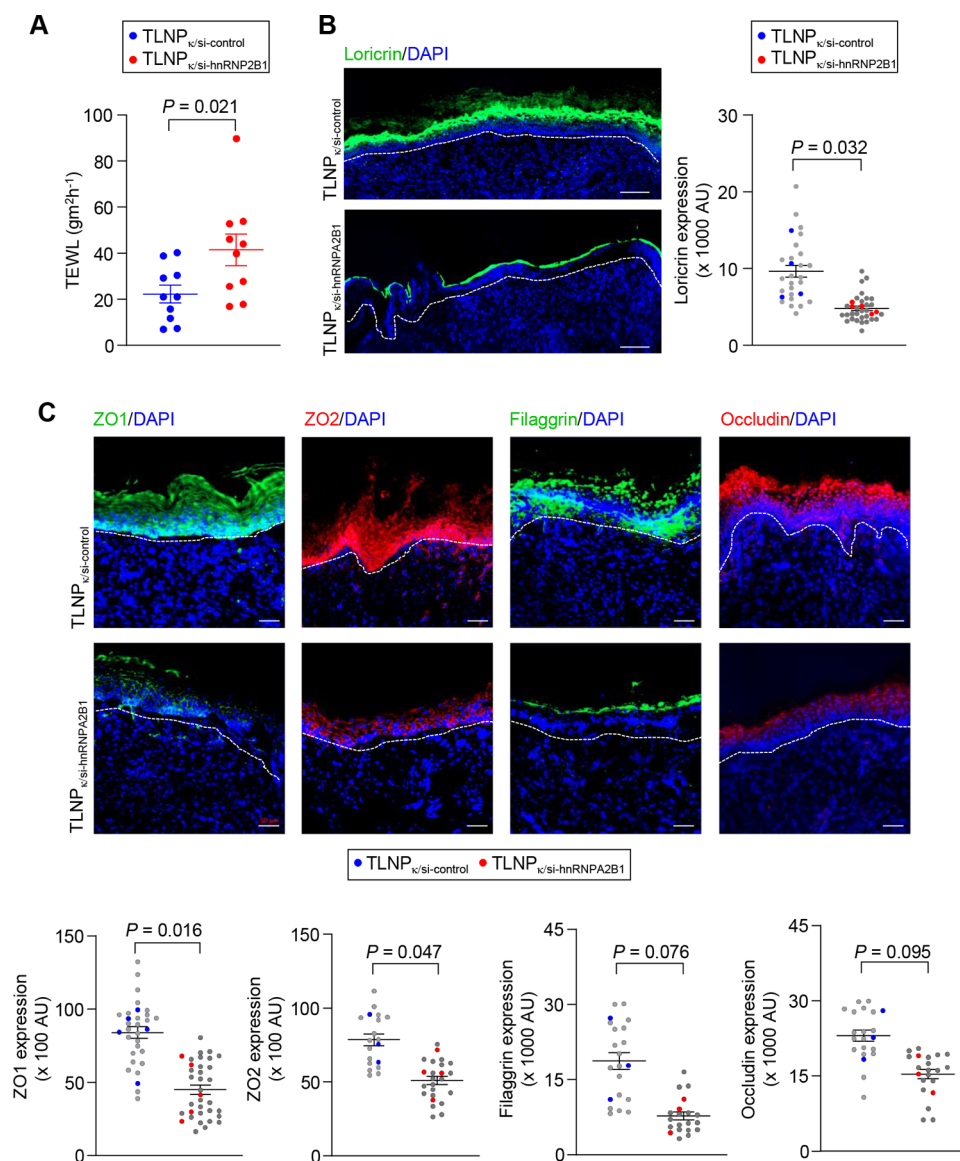


Figure 9. Delivery of keratinocyte-targeted lipid nanoparticles encapsulating si-hnRNPA2B1 compromised the quality of wound closure. (A) Transepidermal water loss (TEWL) after C57BL/6 mice treated with TLNP $_{\kappa}$  encapsulating either si-control or si-hnRNPA2B1 ( $n = 10$ ). (B) Representative co-immunofluorescence staining of loricrin with DAPI counterstaining in wound-edge tissue at day 10 postwounding in C57BL/6 mice treated with either scramble or si-hnRNPA2B1 encapsulated keratinocyte-targeted lipid nanoparticles. Scale, 200  $\mu\text{m}$ . Quantification of loricrin intensity in wound-edge tissue at day 10 postwounding. Each dot corresponds to one quantified ROI, except the blue and red dots, which correspond to the mean of each mouse. At least 5 ROI per mouse ( $n = 4$ ). (C) TLNP $_{\kappa}$ /si-hnRNPA2B1 treatment compromised the expression of ZO-1 (green), ZO-2 (red), filaggrin (green), and occludin (red) in murine skin at day 10. Sections were counterstained with DAPI (blue). The dermal–epidermal junction is indicated by a dashed white line. Scale bars, 50  $\mu\text{m}$ . The abundance of junctional proteins was quantified. Each dot corresponds to one quantified ROI, except the blue and red dots, which correspond to the mean of each mouse. At least 5 ROI per mouse ( $n = 3, 4$ ). Data were expressed as mean  $\pm$  SEM and were analyzed by two-tailed unpaired Student's  $t$  test.

**Delivery of Keratinocyte-Specific Lipid Nanoparticles Encapsulating si-hnRNPA2B1 Compromised Quality of Wound Closure.** Based on observations from *in vitro* studies on

the role of Exo $_{\kappa}$ -GFP in the conversion of macrophage phenotype (Figure S3E), we postulated that *in vivo* delivery of TLNP $_{\kappa}$ /si-hnRNPA2B1 to inhibit miRNA packaging in keratinocytes

will compromise the quality of wound healing in mice. Comparable to findings of *in vitro* studies, delivery of TLNP<sub>κ/si-hnRNPA2B1</sub> to murine keratinocyte significantly suppressed hnRNPA2B1 expression (Figure 8A–D, Figure S6A). Interestingly, no significant difference in the number of exosomes released at the wound edge was observed (Figure S6B). Furthermore, wound closure in both TLNP<sub>κ/si-control</sub> and TLNP<sub>κ/si-hnRNPA2B1</sub> groups was comparable (Figure 8E, Figure S6C,D). However, at day 10 in mice treated with TLNP<sub>κ/si-hnRNPA2B1</sub>, persistent accumulation of inflammatory cells was noted in the granulation tissue (Figure 8F). These inflammatory cells were identified to be as *ωmφ* (Figure 8G, Figure S6E). Unlike the scanty *ωmφ* that exhibit proresolution marker arginase in the TLNP<sub>κ/si-control</sub> group, these *ωmφ* abundant in the TLNP<sub>κ/si-hnRNPA2B1</sub> treated group expressed proinflammatory marker iNOS even at day 10 post-wounding (Figure 8H,I, Figure S6F,G). Such increased abundance of *ωmφ* in the granulation tissue of the TLNP<sub>κ/si-hnRNPA2B1</sub> treated group may not be attributed to increased recruitment on the basis of comparable neutrophil or macrophage counts on day 3 post-wounding (Figure S7). These *ωmφ*, exhibiting the proinflammatory phenotype, persisted in the repaired skin even after the wound was closed following TLNP<sub>κ/si-hnRNPA2B1</sub> treatment (Figure S8). Such a presence of proinflammatory *ωmφ* at the granulation tissue in mice treated with TLNP<sub>κ/si-hnRNPA2B1</sub> lends credence to the notion that the cues for conversion of *ωmφ* from proinflammatory to proresolution state come as miRNA packaged in keratinocyte-derived exosomes.

To investigate the significance of abundant proinflammatory *ωmφ* in the day 10 granulation tissue of TLNP<sub>κ/si-hnRNPA2B1</sub> treated mice, we tested the functional property of the re-epithelialized skin by measuring the barrier function postclosure. The barrier function of the TLNP<sub>κ/si-hnRNPA2B1</sub> group was significantly compromised, demonstrating that indeed wound closure was impaired (Figure 9A). Restoration of the barrier function of the repaired skin is a necessary component of functional wound healing.<sup>44,47–49</sup> The terminally differentiating structural protein loricrin forms 70–80% of the cornified envelope that contributes to the protective barrier function of skin.<sup>49–51</sup> The abundance of loricrin in the re-epithelialized skin was significantly compromised following TLNP<sub>κ/si-hnRNPA2B1</sub> treatment (Figure 9B). Furthermore, lower expression of other junctional proteins such as ZO-1, ZO-2, filaggrin, and occludins was also observed at day 10 postwounding in the TLNP<sub>κ/si-hnRNPA2B1</sub> treated group compared to the TLNP<sub>κ/si-control</sub> group (Figure 9C). Taken together, these observations explain how functional wound closure is impaired in mice treated with TLNP<sub>κ/si-hnRNPA2B1</sub>. Thus, impairment in miRNA packaging in keratinocyte exosomes of the skin impaired resolution of inflammation and compromised functional wound closure.

## CONCLUSION

In summary, we developed a method of isolating Exo<sub>κ-GFP</sub> in tissue for studying keratinocyte–exosome crosstalk during wound healing. This work provides critical insight into the significance of Exo<sub>κ-GFP</sub> in the resolution of wound inflammation and determination of functional wound closure. Exo<sub>κ-GFP</sub> showed an abundance of small bp RNA (<100 bp) in day 5 wound-edge tissue. Exo<sub>κ</sub>-borne miRNA signals enable crosstalk between resident keratinocytes of the skin with visiting *ωmφ*. Glycan ions with high mannose were only detected in wound-edge Exo<sub>κ</sub>. Wound macrophages are known to possess mannose

receptors. Mannose functionalization is commonly used to target nanoparticles for *ωmφ* uptake. In this work, Exo<sub>κ</sub> were taken up by *ωmφ* in the wound-edge tissue. Such uptake caused phenotypic changes in *ωmφ* consistent with the resolution of inflammation. Blockade of miRNA transfer via Exo<sub>κ-GFP</sub> to *ωmφ* by knocking down hnRNPA2B1 caused persistence of proinflammatory *ωmφ*. Thus, exosomal miRNA packaging in skin keratinocytes modifies the wound inflammation response. Impaired resolution of wound inflammation, caused as above, hindered functional wound healing by compromising restoration of the skin barrier function at the site of repair. Findings of this work lay the framework of an emerging paradigm wherein exosome-borne molecular signals drive crosstalk between different cellular compartments in a way that directly determines the fate of wound healing outcomes. Such advancement in our understanding of wound healing unveils heretofore unknown therapeutic targets that may be exploited to design productive wound-care strategies.

## METHODS

**Cells and Cell Culture.** Immortalized human keratinocytes (HaCaT) were grown in Dulbecco's low-glucose (1g/L) modified Eagle's medium (Life Technologies, Gaithersburg, MD) as described previously.<sup>52</sup> Human dermal microvascular endothelial cells (HMECs) were cultured in MCDB-131 medium supplemented 10 mm L-glutamine, and 100 IU/mL of penicillin, 0.1 mg/mL of streptomycin (Invitrogen), as described previously.<sup>53</sup> Human skin fibroblast BJ cells (ATCC CRL-2522) were obtained from ATCC and were cultured in Eagle's Minimum Essential Medium (Catalog No. 30-2003) as per the instruction provided. Mouse keratinocytes (KERA-308) were purchased from Cell Line Services (CLS Germany) and were cultured in Dulbecco's high-glucose (4.5 g/L) modified Eagle's medium (Life Technologies, Gaithersburg, MD). Primary mouse embryonic fibroblasts were purchased from Millipore Sigma (PMEF-HL) and were cultured as per the manufacturer's instruction. For isolation of wound macrophages (*ωmφ*), circular (8 mm) sterile poly(vinyl alcohol) (PVA) sponges were implanted subcutaneously on the backs of 8–12-week-old mice.<sup>54</sup> Sponge-infiltrated wound *mφ* (CD11b<sup>+</sup>) were obtained from day 3 wound cell infiltrate by magnetic-bead-based sorting as previously described.<sup>55,56</sup> The isolated cells were cultured in RPMI-1640 media. The cells were maintained in a standard culture incubator with humidified air containing 5% CO<sub>2</sub> supplemented with 10% FBS and 1% antibiotic–antimycotic (AA) (Life Technologies) unless stated otherwise. All experiments involving isolation or uptake of exosomes were performed with exosome depleted FBS.

**Isolation of Exosome from Cell Culture Media (EV-TRACK ID: EV190103).** Cell culture supernatant (using cells cultured with media described above and 10% Gibco Exosome-Depleted FBS (Thermo-Fisher Scientific)) was centrifuged at 3400g for 15 min, and the supernatant was collected. Extracellular vesicles were isolated from the supernatant using differential ultracentrifugation (Beckman Coulter Optima Max-XP Ultracentrifuge, rotor TLA120.2), as described in Figure S1. Pellets were washed by resuspending in PBS and repelleting via a second round of ultracentrifugation. These pellets were then resuspended in PBS and incubated overnight at 4 °C with magnetic CD9, CD63, and CD81 Dynabeads (Invitrogen). The exosomes attached to the beads were magnetically separated from flow through using a magnetic microcolumn ( $\mu$  column from Miltenyi Biotec MACS). The flow through eluent (membrane particles and apoptotic bodies) was kept and repelleted for further analysis (2 h at 245,000g). For Western blot and flow cytometry, the exosomes were not removed from the magnetic beads. For nanoparticle tracking analysis, TEM or SEM imaging, exosomes were eluted from the beads using elution buffer (ExoFlow Exosome Elution Buffer, System Biosciences) as per the manufacturer's protocol. This method was submitted to EV track.<sup>27</sup>

**Isolation of Keratinocyte-Derived Exosome from Murine Tissue.** EVs and keratinocyte-derived exosomes were isolated from mouse tissue following transfection with Keratin 14 promoter driven

plasmids encoding murine CD63, CD9, and CD 81 with GFP-reporter "in frame". The murine skin and wound-edge tissue were collected and homogenized, suspended in PBS, and vortexed to release exosomes from tissue. The solution was briefly centrifuged and the supernate collected and centrifuged at 5000g for 15 min followed by 20,000g for 45 min. The supernatant was incubated overnight at 4 °C with GFP-trap magnetic agarose beads (Chromotek Catalog # gtma-100) (12  $\mu$ L of GFP-Trap beads/0.15 g of tissue). Exosome isolation from GFP-Trap beads utilized magnets to isolate the beads, enabling the eluent to be removed. The GFP-Trap beads were washed three times in PBS. Finally, elution of intact beads was accomplished by mixing with glycine (0.2 M, pH 3) for 30 s, a process that was repeated five times. The pH was adjusted to 7.4 using 1.0 M Tris, and EXO<sub>K-GFP</sub> pellets were collected by ultracentrifugation (2 h at 245,000g). The flow through was next incubated with magnetic pan-CD beads (Miltenyi Biotec Catalog # 130-117-039) for 2 h at room temperature that were isolated from flow through to recover the non-keratinocyte-derived exosome as described above for Invitrogen Dynabeads.

**Fluorescence Correlation Spectroscopy (FCS).** Exosome–protein binding was also measured by the change in diffusion and anisotropy of a fluorescently labeled antibody (TSG101-PE) incubated in the presence of exosomes or other extracellular vesicles using a two-channel fluorescence correlation spectroscopy system (Confocor 2, Zeiss) attached to an Axiovert200 M inverted microscope (Zeiss).<sup>57</sup> The system measures a characteristic diffusion time ( $\tau_D$ ) of a fluorophore as determined by fitting fluorescent decay within a confocal volume to an autocorrelation curve using eq 1, where  $N$  is the particle concentration and  $Q$  is a factor relating to the ellipticity of the confocal volume:<sup>58</sup>

$$G(t) = 1 + \frac{1}{N_{\text{avg}}} \left( \frac{1}{1 + \tau/\tau_D} \right) \left( \frac{1}{\sqrt{1 + (1/Q^2)(\tau/\tau_D)}} \right) \quad (1)$$

Autocorrelation best fit curves identify the change in particle diffusion with curves shifted to the left, demonstrating faster diffusion (smaller  $\tau_D$ ); exemplary best fit curves are shown, where the curves are fitted using a one-component fit identifying an average characteristic diffusion time for the fluorophores. For fluorophores bound to exosomes, this will provide qualitative evidence of exosomal binding.

**Fluorescence Anisotropy.** Fluorescence anisotropy experiments were conducted using a two-channel fluorescence correlation system where both channels are equipped with crossed analyzers, one perpendicular and one parallel to the emitted laser light. The emitted light divides into two separate beams of equal intensity, which are guided into each of the two APD channels. The anisotropy can be calculated using eq 2

$$r = (I_1 - I_2)/(I_1 + 2I_2) \quad (2)$$

where  $I_1$  and  $I_2$  are the intensities of the parallel and perpendicular channels, respectively.<sup>57,59</sup> A correction factor for the difference in analyzer sensitivity was not utilized, as this factor does not alter the significance of the change in anisotropy between different conditions. Anisotropy experiments are complementary to autocorrelation analysis because they provide information about the short-range mobility of the tracer molecules, namely, the change in rotational diffusion. The autocorrelation curves shown are examples of curves collected with the concentration normalized; anisotropy data were collected using 10 s runs for each data point.

**N-Glycan Analysis.** Denaturation solution, consisting of 0.1% SDS (Bio-Rad Laboratories, Inc., Hercules, CA) and 0.2%  $\beta$ -mercaptoethanol (Sigma-Aldrich, St. Louis, MO) in 50 mM sodium phosphate buffer (pH 7.5), was added to the exosome sample and incubated at 60 °C for 1 h. After that, nonidet P40 substitute (NP-40, Roche Diagnostics Corp, Indianapolis, IN) was added to encapsulate SDS. The sample was then incubated with peptide *N*-glycosidase F (PNGase F, New England BioLabs, Inc., Ipswich, MA) at 37 °C for 18 h. Cleaved N-glycans were purified through solid-phase extraction on an active charcoal phase (Micro SpinColumns, Harvard Apparatus, Holliston, MA). For methylamidation,<sup>60,61</sup> purified and dried glycans were dissolved in 5

$\mu$ L of DMSO (Fisher Chemical, Fair Lawn, NJ), containing 2 M methylamine hydrochloride (Sigma-Aldrich, St. Louis, MO), 1 M 4-methylmorpholine (Sigma-Aldrich, St. Louis, MO), and 5  $\mu$ L of 100 mM (7-azabenzotriazol-1-yloxy) tripyrrolidinophosphonium hexafluorophosphate (PyAOP, Sigma-Aldrich, St. Louis, MO). The reaction proceeded at room temperature in the dark for 4 h and was terminated with addition of 240  $\mu$ L of 85% acetonitrile (OmniSolv, Billerica, MA). Methylamidated N-glycans were purified through solid-phase extraction on a hydrophilic interaction phase (Amino Micro SpinColumns, Harvard Apparatus, Holliston, MA). To impart a +1 charge for electrophoresis, glycans were labeled with Girard's reagent T (GT; Sigma-Aldrich, St. Louis, MO). Briefly, 25  $\mu$ L of 0.02 M GT in 10% (v/v) acetic acid was added to purified glycans and incubated at 55 °C for 4 h, and the reaction mixture was dried in a CentriVap concentrator to remove excess acetic acid and water.

CE-MS analysis<sup>35</sup> of the N-glycans was conducted on a CESI 8000 instrument (SCIEX Separations, Framingham, MA) with a neutral capillary cartridge (30  $\mu$ m i.d.  $\times$  90 cm length; Opti-MS, B07368, SCIEX Separations) and an Orbitrap Fusion Lumos mass spectrometer (Thermo Fisher, Waltham, MA). GT-labeled N-glycans were dissolved in 10  $\mu$ L of 0.5% acetic acid (v/v). Sample was injected into the capillary hydrostatically at 3 psi for 25 s and electrophoretically separated with an applied potential of 25 kV and a pressure of 3 psi. The capillary was connected to the mass spectrometer through an electrospray interface with an applied potential of 1090 V. MS data from positive ions ranging from 200 to 2000  $m/z$  were collected. The detected masses were searched on ExPASy GlycoMod, and tentative structures were assigned based on previously reported structures on ExPASy GlyConnect. Relative intensities of the N-glycans were calculated with the Thermo Xcalibur Qual Browser algorithm Genesis where the signal was boxcar averaged (7 points) with a mass tolerance of 30 ppm.

**Flow Cytometry.** Exosome markers were assessed using PE anti-TSG101 (1:100, NB200-112PE, Novus Biologicals) and PE anti-flotillin-1 (1:200, ab225165, Abcam) by incubating the antibodies at the noted concentrations with the beads for 90 min at room temperature. Additional exosome markers, anti-Alix (1:100, 92880 Cell Signaling Technology), and anti-HSP90 (1:100, ab59459, Abcam) were first incubated with beads for 90 min at room temperature followed by magnetic separation using PBS to remove excess antibodies and incubation of beads next with the secondary antibody, goat Anti-Rabbit IgG Alexa Fluor 488 (1:200, ab150077). PE fluorescence was determined using the PE channel. Alexa Fluor 488 fluorescence was determined using the FITC channel.

For the membrane integrity assay, human keratinocytes were incubated with propidium iodide (1 mg/mL) and the percentage of viable cells was measured in the FL2 channel.<sup>62</sup> Heat killed human keratinocytes were used as the positive control. Samples were run on an Accuri C6 flow cytometer (Accuri Cytometers, MI, USA) or LSRFortessa X-20 flow cytometers (BD Biosciences, CA, USA). Data were collected from 5000–10,000 events at a flow rate of 250–300 events/s and analyzed using FlowJo software (Tree Star, OR, USA).

**Synthesis of DSPE-PEG<sub>2000</sub>-ASG33.** DSPE-PEG<sub>2000</sub>-ASG33 was synthesized through the conjugation of ASG33<sup>44</sup> (sequence: ASKA-IQVFLLAG, Genscript, NJ, USA) and DSPE-PEG<sub>2000</sub>-NHS (Nanocs, Boston, MA, USA). Lipid peptide conjugation was done by dissolving 20 mg of DSPE-PEG<sub>2000</sub>-NHS in dimethyl sulfoxide (DMSO) with a solution of ASG33 in DMSO and 10  $\mu$ L of trimethylamine (TEA). The reaction was performed in an oxygen-free environment (nitrogen purge) at room temperature for 24 h. The resulting mixture was dialyzed against deionized water using a slide-a-lyzer dialysis cassette (molecular weight cutoff, MWCO 3500) for 48 h to remove impurities. The final solution was lyophilized, and the powder was stored at –20 °C for further use. DSPE-PEG<sub>2000</sub>-ASG33 was characterized using MALDI-TOF mass spectrometry (15 T FT-ICR Bruker Daltonics Inc.).

**Preparation of Keratinocyte-Targeted Lipid Nanoparticles (TLNP<sub>k</sub>).** TLNP<sub>k</sub> were prepared by using a modified ethanol dilution method as described previously.<sup>44</sup> Briefly, DOTAP/DODMA/DOPC/DSPE-PEG<sub>2000</sub>-ASG33/Tween80 (20/30/27/3/20, mol/mol) were dissolved in ethanol and mixed with siRNA in triethylammonium

acetate buffer (20 mM, pH 4.5). The mixture was further diluted using PBS (10 mM phosphate, 135 mM NaCl, pH 7.4). The ethanol and free siRNA were removed by dialysis using a slide-a-lyzer dialysis cassette (molecular weight cutoff, MWCO 20000). DSPE-PEG<sub>2000</sub>-A5G33 was replaced with DSPE-PEG<sub>2000</sub> in the nontargeted lipid nanoparticles (non-TLNP<sub>κ</sub>). If lipophilic fluorescence dye DiD were chosen to label the LNPs, 0.2% mol/mol amount of dye was added into the above formulation recipe.

**Encapsulation Efficiency of TLNP<sub>κ</sub>.** Encapsulation efficiency was performed by the Quant-iT RiboGreen RNA Kit (Invitrogen, Grand Island, NY, USA) as described previously.<sup>44</sup> The unencapsulated siRNA content and the total siRNA content that was obtained upon lysis of the TLNP<sub>κ</sub> by 1% Triton were determined according to the manufacturer's instruction using Multi-Mode Microplate Readers (Biotek, Winooski, VT, USA) at 480 nm  $\lambda_{\text{ex}}$  and 520 nm  $\lambda_{\text{em}}$ . The encapsulation efficiency (EE) of siRNA was calculated with the following equation:

$$\text{EE} = \frac{\text{Total siRNA} - \text{Unencapsulated siRNA}}{\text{Total siRNA}} \times 100\%$$

The encapsulation efficiency of siRNA encapsulated keratinocyte-targeted lipid nanoparticles (TLNP<sub>κ/si</sub>) was also verified using gel retardation assay via 1% agarose gel. Electrophoresis was performed at 100 V for 20 min and visualized under a UV transilluminator (Bio-Rad laboratories, CA, USA).

**Electron Microscopy.** The morphology of exosomes and TLNP<sub>κ/si-hnRNPA2B1</sub> was observed by transition electron microscopy (TEM, Japan). Briefly, the particles were ultracentrifuged at 250,000g at 4 °C; then, the pellet was dispersed into deionized water and dropped on a copper grid, stained with NanoVan (vanadium-based negative stain from Nanoprobes.com, Yaphank, New York), and viewed on a Tecnai G2 12 Bio Twin electron microscope (FEI, Hillsboro, OR, USA) at the Electron Microscopy Center at the Indiana University School of Medicine.

The morphology of exosomes and other EVs was checked by scanning electron microscopy. Briefly, pellets containing either exosomes or eluent were resuspended in ddH<sub>2</sub>O with 0.1% formalin or other buffer and dropped onto clean silica wafers. After drying, samples were desiccated in a vacuum chamber for at least 12 h before analysis. Images were obtained after gold sputter coating using a field emission scanning electron microscope (JEOL 7800F, JEOL Japan) at a beam energy of 5 or 10 kV.

**Nanoparticle Tracking Analysis.** The mean particle diameter and concentration of extracellular vesicles and TLNP<sub>κ</sub> were analyzed by a Nanosight NS300 instrument with a 532 nm laser and sCMOS camera (Malvern, Worcestershire, U.K.) as previously described.<sup>44</sup> Briefly, samples were diluted to 100:1 or as needed in fresh Milli-Q to obtain 5–100 particles/frame. Samples were typically analyzed using five runs of 30 s collecting 25 frames per second (749 frames per run) with viscosity determined by the highest available temperature and camera level for the sample (typically 15 or 14). The syringe pump speed was 60. NTA automatically compensates for flow in the sample, so only Brownian motion is used for size determination. For processing results, the detection threshold was typically 5 with automated blur size and max jump distance. Standard 100 nm latex spheres were run at 1000:1 dilution in Milli-Q to check the instrument performance. Data were analyzed by NTA 3.0 software (Malvern Instruments).

**Zeta Potential Analysis.** Surface charge ( $\zeta$  potential) measurement of TLNP<sub>κ</sub> was determined by a Zetasizer (Nano-Z, Malvern Instruments Ltd., U.K.). All samples were dispersed in double-distilled water and tested in volume-weighted size distribution mode. Aliquots of TLNP<sub>κ</sub> containing anti-miR-107 were diluted in PBS with a series of pHs (50 mM, from 2 to 11) to determine the pH dependency of surface charge.

**LDH Release Assay.** Cytotoxicity of TLNP<sub>κ</sub> was analyzed by measuring the lactate dehydrogenase (LDH) leakage in the media using the TOX-7 *in vitro* toxicology kit (Sigma, St. Louis, MO) as previously described.<sup>63</sup> Briefly, HaCaT cells were seeded in 12-well plates (0.1 × 10<sup>6</sup> cells/well) and incubated overnight. The media were changed when the cells were treated with TLNP<sub>κ/si-hnRNPA2B1</sub>. After incubation for the

designated time (24 and 48 h), cell culture media were collected and centrifuged; then, the supernatant was transferred to a 96-well plate and incubated with the mixture of the assay substrate, enzyme, and dye solutions for 20–30 min in the dark at room temperature. The reaction was terminated by adding 1 N HCl to each well. LDH absorbance was measured at 490 nm using the Bio-TEK ELX 808 IU micro plate reader (Bio-TEK Instruments, Inc, Winooski, VT).

**MTT Assay.** The viability of keratinocytes post nanoparticle treatment was measured using a Vybrant MTT Cell Proliferation Assay Kit (Thermo Fisher Scientific) per the manufacturer's instructions. At 24 h after treatment, cells were incubated in medium containing 3-(4,5-dimethylthiazol-2-yl)-2,5-diphenyltetrazolium bromide (MTT) for 4–6 h at 37 °C with 5% CO<sub>2</sub>. After MTT treatment, medium was removed, and DMSO was added (10–20 min at 37 °C with 5% CO<sub>2</sub>) to solubilize formazan produced as a result of MTT metabolism. DMSO extract from each well (100  $\mu$ L) was collected in a 96-well plate, and formazan content was determined by reading the absorbance at 540 nm.<sup>64</sup>

**Lipid Nanoparticles and Exosome Uptake Assay.** For the cellular uptake of keratinocyte-targeted lipid nanoparticle studies, a mixed culture of three different cells was performed. 1 × 10<sup>5</sup> cells (HaCaT:HMEC:BJ1 = 1:1:3) were seeded in a 12-well plate in mixed media with 10% FBS and 1% antibiotics and incubated overnight. DiD-loaded TLNP<sub>κ/si-hnRNPA2B1</sub> and non-TLNP<sub>κ/si-hnRNPA2B1</sub> were prepared and added into the cells and then incubated at 37 °C. After 2 h, cells were washed using PBS and fixed with 4% paraformaldehyde for 15 min at room temperature. HaCaT cells and HMEC were immunostained by K14 and CD31, respectively. Confocal images were acquired with a confocal-laser-scanning system (CARL ZEISS confocal microscope LSM 888). For live imaging of the uptake of TLNP<sub>κ</sub> by Kera 308, Kera cells were seeded in four-well tissue culture chambers at a density of 2 × 10<sup>4</sup> cells and incubated overnight. DiD-loaded TLNP<sub>κ/FAM-siRNA</sub> and non-TLNP<sub>κ/FAM-siRNA</sub> were prepared and incubated with the cells. The cellular uptake was visualized for about 95 min.

For uptake of exosome studies by wound macrophages, Exo<sub>κ-GFP</sub> were isolated from murine skin. The concentration of the exosome was measured by nanoparticle tracking analysis. The exosomes were stained with DiO and added to the day 3  $\omega$ m $\phi$ , and live cell imaging was performed. For blocking the C-type lectin receptors, a cocktail of neutralizing antibodies was used. Murine mincle (Mabg-mmcl; Sigma), mouse dectin 1 (MAB17561; R&D systems), and mouse SIGNR1 (AF18836; R&D systems) were used.

**Ultrahigh-Resolution Fourier Transform Mass Spectrometry.** The accurate mass of the samples was determined using mass spectrometry. High-resolution mass spectrometry analyses were carried out at The Ohio State University Campus Chemical Instrument Center's Mass Spectrometry and Proteomics Facility (OSU CCIC MSP) by using a 15 T Bruker Solarix FT-ICR instrument (Bruker Daltonics, Billerica, MA).<sup>65</sup> Matrix-assisted laser desorption/ionization (MALDI) was used with the alpha cyano hydroxycinnamic acid (HCCA) matrix in the positive ion mode. The matrix was purchased from Bruker Daltonics (Billerica, MA). The third harmonic of a Yag/Nd laser was used (351 nm) for MALDI with a 25% laser power. The samples were mixed with the saturated solution of the HCCA matrix with a matrix:analyte ratio of around 100:1. The resolution of the FT-ICR instrument was set to 150,000 at around  $m/z$  2500. The detection range was  $m/z$  300–13,000, but no ions were observed beyond  $m/z$  5000. Standard FT-ICR ion optics parameters were used to maximize the ion detection efficiency in the applied  $m/z$  range.

**Transfection of XmiR-21 Mimics.** DharmaFECT 1 transfection reagent was employed to transfect HaCaT cells with XmiR-21 (100 nM) (Dharmacon) as described previously.<sup>49</sup> Cells and media were collected 48 h after transfection for further analysis, as indicated.

**Animals.** Male C57BL/6 mice (aged 8–10 weeks) were obtained from Jackson Laboratory. All animal studies were performed in accordance with protocols approved by the Laboratory Animal Resource Center of Indiana University. No statistical methods were used to predetermine the sample size. Power analysis was not necessary for this study. The animals were tagged and grouped randomly using a computer-based algorithm ([www.random.org](http://www.random.org)).

**Wound Models and *in Vivo* TLNP<sub>κ</sub>/siRNA Delivery.** For wounding, two 6 mm diameter full-thickness excisional wounds were developed on the dorsal skin of mice with a 6 mm disposable biopsy punch and splinted with a silicon sheet to prevent contraction, thereby allowing wounds to heal through granulation and re-epithelialization.<sup>66–68</sup> TLNP<sub>κ</sub>/si-control and TLNP<sub>κ</sub>/si-hnRNPA2B1 were administered into the wound edge by subcutaneous injection. For isolation of exosomes from the wound edge, four 8 mm diameter full-thickness excisional wounds were developed on the dorsal skin of mice with an 8 mm disposable biopsy punch without any stent. During the wounding procedure, mice were anesthetized by low-dose isoflurane (1.5%–2%) inhalation as per the standard recommendation. Tissue from the wounds (skin) was snap-frozen and stored at –80 °C until harvested for exosome collection described above. Each wound was digitally photographed at the time point indicated. Wound size was calculated by the ImageJ software.<sup>22</sup>

The animals were euthanized at the indicated time, and wound edges were collected for analyses. For wound-edge harvest, 1–1.5 mm of the tissue from the leading edge of the wounded skin was excised around the entire wound. The tissues were snap-frozen and, if used for exosome harvest, left at –80 °C until harvested for the exosome collection described above. If used for IHC, tissues were collected either in 4% paraformaldehyde or in optimal cutting temperature (OCT) compound.

**Tissue Nanotransfection 2.0.** *In vivo* TNT was performed as described previously with a modification in the chip design.<sup>31</sup> The hollow microneedle array was fabricated on a double side polished silicon wafer using a standard semiconductor process in a cleanroom environment. First, the Si wafer was wet oxidized in a furnace at 1150 °C to grow 4 μm thermal oxide on both sides that served as a hard mask during the deep silicon etching. A 10 μm thick, positive photoresist of AZ 9260 was spin-coated on one side of the silicon wafer followed by a prebake at 110 °C for 10 min. A direct laser writing system was used to expose a layout of 25 μm circle arrays followed by development in a diluted AZ400K solution to remove the exposed area. The 4 μm oxide was removed by a plasma etcher using CHF<sub>3</sub> chemistry. The wafer was then transferred to another plasma etching system to perform a deep Si etching called the Bosch process, a common semiconductor process to achieve a vertical etching profile with a high aspect ratio. After silicon etching of about 350–450 μm in depth to form the reservoir arrays, the wafer was flipped for the next step to etch the hollow microneedle arrays. A donut-shaped pattern was exposed onto the resist, and the pattern was transferred to the oxide using the same set of steps mentioned above. Then, the wafer was etched by the Bosch process until the hollow microneedles were connected to the reservoirs so that the cargo or the plasmid DNA fluid could freely flow from the reservoir to the hollow microchannel. The SEM images showed the fabricated silicon hollow microneedle array (Figure 1C) that has a length of 170 μm, an outer diameter of 50 μm, and a hollow diameter of 4 μm. When an electric pulse was applied between the TNT chip and the tissue, the negatively charged plasma DNA would travel from the reservoir to nearby target cells by electrophoresis and enter them by electro-poration. To test the TNT2.0 delivery efficiency, FAM-DNA (5′/56-FAM/TACCGCTGCGACCCTCT-3′) was used in murine skin.

**Trans-Epidermal Water Loss.** TEWL serves as a reliable index to evaluate the skin barrier function *in vivo*.<sup>23–25</sup> TEWL was measured from the skin and wounds using a DermaLab TEWL Probe (cyberDERM, Broomall, PA). The data were expressed in g·m<sup>-2</sup>·h<sup>-1</sup>.

**RNA Extraction and Quantitative Real-Time PCR.** RNA from cells or exosomes was extracted using a miRVana miRNA isolation kit (Ambion) according to the manufacturer's protocol.<sup>21,69</sup> For determination of miR expression, specific TaqMan assays for miRs and the TaqMan miRNA reverse transcription kit were used, followed by real-time PCR using the Universal PCR Master Mix (Applied Biosystems, Foster City, CA). mRNA was quantified by real-time or quantitative (Q) PCR assay using the double-stranded DNA binding dye SYBR Green-I.<sup>21,69</sup>

**High-Resolution Automated Electrophoresis of RNA.** The RNA isolated from Exo<sub>κ</sub>-GFP was analyzed in an Agilent 2100 Bioanalyzer (Agilent Technologies, Santa Clara, California).<sup>70</sup>

**Western Blots.** Western blot was performed using antibodies against human hnRNPA2B1 (Sigma-Aldrich; SAB1403931, 1:500), mouse hnRNPA2B1 (Sigma-Aldrich; HPA001666, 1:200), TSG101 (Abcam; ab125011, 1:1000), Alix (Novus Biologicals; JM 85-31, 1:1000), HSP90 (Abcam; ab59459, 1:1000), Flotillin 1 (Abcam; ab133497, 1:200), GM130 (Abcam; ab52649, 1:1000), and Prohibitin (Abcam; ab28172, 1:200). The signal was visualized using the corresponding HRP-conjugated secondary antibody (Amersham, 1:3,000) and ECL Plus Western Blotting Detection Reagents (Amersham). β-Actin (Sigma-Aldrich; A5441, 1:2000) served as a loading control.<sup>21,22</sup>

**Immunohistochemistry (IHC) and Microscopy.** Immunohistochemistry was performed as described previously.<sup>71</sup> Immunostainings of F4/80 (Bio-Rad, MCA497R; 1:200), K14 (Covance, PRB-155P-100; 1:400), GFP (Abcam, ab13970; 1:500), MPO (Abcam, ab9535; 1:50), arginase (Abcam; 203490, 1:100), iNOS (Abcam; ab115819, 1:100), hnRNPA2B1 (Sigma-Aldrich; HPA001666, 1:50), Occludin (Invitrogen, 711500; 1:200), ZO-1 (Invitrogen, 617300; 1:200), ZO-2 (Invitrogen, 389100; 1:200), Loricrin (Biolegend, PRB-145P; 1:400), Filaggrin (Covance, PRB-417P; 1:500), CD31 (BD Pharmingen, 550274; 1:400), Col1A2 (Santa Cruz, sc-393573; 1:200), and CDH5 (Abcam; ab91064, 1:200) were performed on paraffin and cryosections of skin sample using specific antibodies as indicated.<sup>57</sup> The specificity of the antibodies was validated using rabbit isotype control (Abcam, ab27478; 1:400). Briefly, the sections were blocked with 10% normal goat serum and incubated with specific antibodies overnight at 4 °C. The signal was visualized by subsequent incubation with fluorescence-tagged appropriate secondary antibodies (Alexa 488-tagged α-rabbit, 1:200; Alexa 568-tagged α-rabbit, 1:200; Alexa 568-tagged α-rat, 1:200; Alexa 488-tagged α-chicken, 1:200; Alexa 568 α-mouse, 1:200) and counter stained with DAPI. Images were captured by a microscope using a super-resolution airyscan laser-scanning confocal system (CARL ZEISS confocal microscope LSM 888 and Axio Scan.Z1, Zeiss, Germany). Quantification of the fluorescent intensity of an image was analyzed using Zen software (Zen blue 3.1) and ImageJ software with the colocalization plugin.<sup>72,73</sup>

**Statistical Analysis.** GraphPad Prism (GraphPad Software) v8.0 was used for statistical analyses. No statistical methods were used to predetermine the sample size. The ΔΔC<sub>t</sub> value was used for statistical analysis of all RT-qPCR data. Statistical analysis between multiple groups was performed using one-way analysis of variance with the *posthoc* Sidak or Bonferroni multiple comparison test. Statistical analysis between two groups was performed using unpaired Student's two-sided *t* tests. *P* < 0.05 was considered statistically significant. Significance levels and exact *P* values were indicated in all relevant figures. Data were assumed to be normally distributed for all analyses conducted. Data for independent experiments were presented as means ± SEM unless otherwise stated.

## ASSOCIATED CONTENT

### Supporting Information

The Supporting Information is available free of charge at <https://pubs.acs.org/doi/10.1021/acsnano.0c03064>.

Isolation and characterization of exosomes from human keratinocyte conditioned culture media (S1); identification and isolation of keratinocyte-derived exosome in murine skin (S2); conversion of wound macrophage phenotype following uptake of keratinocyte-derived exosome (S3); specificity, uptake, and cytotoxicity of human-keratinocyte-targeted lipid nanoparticles (TLNP<sub>κ</sub>) (S4); abundance of miR-21-5p in keratinocytes and exosome after transfection of XmiR-21-5p (S5); delivery of TLNP<sub>κ</sub> encapsulating si-hnRNPA2B1 did not change hnRNPA2B1 expression in other cell types and did not compromise Exo<sub>κ</sub>-GFP abundance or wound closure (S6), did not compromise recruitment of inflammatory cells post-wounding (S7), and results in

persistence of inflammatory cells post-wound closure (S8) (PDF)

N-glycan analysis of exosome isolated from skin and wound-edge tissue (Table S1) (PDF)

Live-cell confocal images showing uptake of non-TLNP<sub>κ</sub> by mouse keratinocytes using LSM 880 (Movie S1) (MP4)

Live-cell confocal images showing uptake of TLNP<sub>κ</sub> by mouse keratinocytes using LSM 880 (Movie S2) (MP4)

Live-cell confocal images showing uptake of Exo<sub>κ</sub>-GFP by mouse wound macrophages without inhibition of C-type lectin using LSM 880 (Movie S3) (MP4)

Live-cell confocal images showing uptake of Exo<sub>κ</sub>-GFP by mouse wound macrophages with inhibition of C-type lectin using LSM 880 (Movie S4) (MP4)

## AUTHOR INFORMATION

### Corresponding Authors

**David E. Clemmer** – Department of Chemistry, Indiana University, Bloomington, Indiana 47405, United States; [orcid.org/0000-0003-4039-1360](https://orcid.org/0000-0003-4039-1360); Phone: 812-855-8259; Email: [clemmer@indiana.edu](mailto:clemmer@indiana.edu)

**Subhadip Ghatak** – Indiana Center for Regenerative Medicine & Engineering, Department of Surgery, Indiana University School of Medicine, Indianapolis, Indiana 46202, United States; [orcid.org/0000-0001-5641-3902](https://orcid.org/0000-0001-5641-3902); Phone: 317-278-2711; Email: [sughatak@iu.edu](mailto:sughatak@iu.edu)

### Authors

**Xiaoju Zhou** – Indiana Center for Regenerative Medicine & Engineering, Department of Surgery, Indiana University School of Medicine, Indianapolis, Indiana 46202, United States; School of Pharmaceutical Sciences, Wuhan University, Wuhan 430071, China; [orcid.org/0000-0003-0797-1312](https://orcid.org/0000-0003-0797-1312)

**Brooke A. Brown** – Department of Chemistry, Indiana University, Bloomington, Indiana 47405, United States

**Amanda P. Siegel** – Indiana Center for Regenerative Medicine & Engineering, Department of Surgery, Indiana University School of Medicine, Indianapolis, Indiana 46202, United States; Integrated Nanosystems Development Institute, Indiana University–Purdue University, Indianapolis, Indiana 46202, United States; [orcid.org/0000-0003-4112-0212](https://orcid.org/0000-0003-4112-0212)

**Mohamed S. El Masry** – Indiana Center for Regenerative Medicine & Engineering, Department of Surgery, Indiana University School of Medicine, Indianapolis, Indiana 46202, United States; Department of Plastic and Reconstructive Surgery, Zagazig University, Zagazig 44519, Egypt; [orcid.org/0000-0002-2686-1509](https://orcid.org/0000-0002-2686-1509)

**Xuyao Zeng** – Department of Chemistry, Indiana University, Bloomington, Indiana 47405, United States

**Woran Song** – Department of Chemistry, Indiana University, Bloomington, Indiana 47405, United States

**Amitava Das** – Indiana Center for Regenerative Medicine & Engineering, Department of Surgery, Indiana University School of Medicine, Indianapolis, Indiana 46202, United States

**Puneet Khandelwal** – Indiana Center for Regenerative Medicine & Engineering, Department of Surgery, Indiana University School of Medicine, Indianapolis, Indiana 46202, United States; [orcid.org/0000-0001-7204-9397](https://orcid.org/0000-0001-7204-9397)

**Andrew Clark** – Indiana Center for Regenerative Medicine & Engineering, Department of Surgery, Indiana University School of Medicine, Indianapolis, Indiana 46202, United States

**Kanhaiya Singh** – Indiana Center for Regenerative Medicine & Engineering, Department of Surgery, Indiana University School of Medicine, Indianapolis, Indiana 46202, United States

**Poornachander R. Guda** – Indiana Center for Regenerative Medicine & Engineering, Department of Surgery, Indiana University School of Medicine, Indianapolis, Indiana 46202, United States; [orcid.org/0000-0003-2295-9637](https://orcid.org/0000-0003-2295-9637)

**Mahadeo Gorain** – Indiana Center for Regenerative Medicine & Engineering, Department of Surgery, Indiana University School of Medicine, Indianapolis, Indiana 46202, United States

**Lava Timsina** – Indiana Center for Regenerative Medicine & Engineering, Department of Surgery and Center for Outcomes Research, Department of Surgery, Indiana University School of Medicine, Indianapolis, Indiana 46202, United States; [orcid.org/0000-0001-7493-5843](https://orcid.org/0000-0001-7493-5843)

**Yi Xuan** – Indiana Center for Regenerative Medicine & Engineering, Department of Surgery, Indiana University School of Medicine, Indianapolis, Indiana 46202, United States; [orcid.org/0000-0003-4795-957X](https://orcid.org/0000-0003-4795-957X)

**Stephen C. Jacobson** – Department of Chemistry, Indiana University, Bloomington, Indiana 47405, United States; [orcid.org/0000-0003-2415-041X](https://orcid.org/0000-0003-2415-041X)

**Milos V. Novotny** – Department of Chemistry, Indiana University, Bloomington, Indiana 47405, United States; [orcid.org/0000-0001-5530-7059](https://orcid.org/0000-0001-5530-7059)

**Sashwati Roy** – Indiana Center for Regenerative Medicine & Engineering, Department of Surgery, Indiana University School of Medicine, Indianapolis, Indiana 46202, United States

**Mangilal Agarwal** – Integrated Nanosystems Development Institute, Indiana University–Purdue University, Indianapolis, Indiana 46202, United States; [orcid.org/0000-0003-3039-0073](https://orcid.org/0000-0003-3039-0073)

**Robert J. Lee** – Division of Pharmaceutics and Pharmacology, The Ohio State University, Columbus, Ohio 43210, United States

**Chandan K. Sen** – Indiana Center for Regenerative Medicine & Engineering, Department of Surgery, Indiana University School of Medicine, Indianapolis, Indiana 46202, United States; [orcid.org/0000-0003-3151-5202](https://orcid.org/0000-0003-3151-5202)

Complete contact information is available at: <https://pubs.acs.org/10.1021/acsnano.0c03064>

### Notes

The authors declare no competing financial interest.

### ACKNOWLEDGMENTS

We would like to acknowledge the Integrated Nanosystems Development Institute (INDI) for use of their JEOL 7800-f Field Emission Scanning Electron Microscope, which was awarded through NSF grant MRI-1229514. The 15 T Bruker SolarixR FT-ICR instrument was supported by NIH Award Number Grant S10 OD018507. This study was primarily supported by junior faculty startup pack from ICRME to S.G. In addition, this study was also supported in part by NR015676 and DK114718 to S.R. and NS042617 to C.K.S. This work also acknowledges the support of Lilly Indiana Collaborative Initiative for Talent Enrichment (INCITE) program.

### REFERENCES

(1) Ahmed, K. A.; Xiang, J. Mechanisms of Cellular Communication through Intercellular Protein Transfer. *J. Cell. Mol. Med.* **2011**, *15*, 1458–73.

- (2) Peinado, H.; Lavotshkin, S.; Lyden, D. The Secreted Factors Responsible for Pre-Metastatic Niche Formation: Old Sayings and New Thoughts. *Semin. Cancer Biol.* **2011**, *21*, 139–46.
- (3) Colombo, M.; Raposo, G.; Thery, C. Biogenesis, Secretion, and Intercellular Interactions of Exosomes and Other Extracellular Vesicles. *Annu. Rev. Cell Dev. Biol.* **2014**, *30*, 255–89.
- (4) Faict, S.; Muller, J.; De Veirman, K.; De Bruyne, E.; Maes, K.; Vrancken, L.; Heusschen, R.; De Raeye, H.; Schots, R.; Vanderkerken, K.; Caers, J.; Menu, E. Exosomes Play a Role in Multiple Myeloma Bone Disease and Tumor Development by Targeting Osteoclasts and Osteoblasts. *Blood Cancer J.* **2018**, *8*, 105.
- (5) Hosseinkhani, B.; Kuypers, S.; van den Akker, N. M. S.; Molin, D. G. M.; Michiels, L. Extracellular Vesicles Work as a Functional Inflammatory Mediator between Vascular Endothelial Cells and Immune Cells. *Front. Immunol.* **2018**, *9*, 1789.
- (6) Wang, J.; Faict, S.; Maes, K.; De Bruyne, E.; Van Valckenborgh, E.; Schots, R.; Vanderkerken, K.; Menu, E. Extracellular Vesicle Cross-Talk in the Bone Marrow Microenvironment: Implications in Multiple Myeloma. *Oncotarget.* **2016**, *7*, 38927–38945.
- (7) Xu, R.; Greening, D. W.; Zhu, H. J.; Takahashi, N.; Simpson, R. J. Extracellular Vesicle Isolation and Characterization: Toward Clinical Application. *J. Clin. Invest.* **2016**, *126*, 1152–62.
- (8) Thery, C.; Ostrowski, M.; Segura, E. Membrane Vesicles as Conveyors of Immune Responses. *Nat. Rev. Immunol.* **2009**, *9*, 581–93.
- (9) Zgheib, C.; Hilton, S. A.; Dewberry, L. C.; Hodges, M. M.; Ghatak, S.; Xu, J.; Singh, S.; Roy, S.; Sen, C. K.; Seal, S.; Liechty, K. W. Use of Cerium Oxide Nanoparticles Conjugated with MicroRNA-146a to Correct the Diabetic Wound Healing Impairment. *J. Am. Coll. Surg.* **2019**, *228*, 107–115.
- (10) Kojima, R.; Bojar, D.; Rizzi, G.; Hamri, G. C.; El-Baba, M. D.; Saxena, P.; Auslander, S.; Tan, K. R.; Fussenegger, M. Designer Exosomes Produced by Implanted Cells Intracerebrally Deliver Therapeutic Cargo for Parkinson's Disease Treatment. *Nat. Commun.* **2018**, *9*, 1305.
- (11) Janas, T.; Janas, M. M.; Sapoń, K.; Janas, T. Mechanisms of RNA Loading into Exosomes. *FEBS Lett.* **2015**, *589*, 1391–1398.
- (12) Creemers, E. E.; Tijssen, A. J.; Pinto, Y. M. Circulating MicroRNAs: Novel Biomarkers and Extracellular Communicators in Cardiovascular Disease? *Circ. Res.* **2012**, *110*, 483–95.
- (13) Guduric-Fuchs, J.; O'Connor, A.; Camp, B.; O'Neill, C. L.; Medina, R. J.; Simpson, D. A. Selective Extracellular Vesicle-Mediated Export of an Overlapping Set of MicroRNAs from Multiple Cell Types. *BMC Genomics* **2012**, *13*, 357.
- (14) Zhang, J.; Li, S.; Li, L.; Li, M.; Guo, C.; Yao, J.; Mi, S. Exosome and Exosomal MicroRNA: Trafficking, Sorting, and Function. *Genomics, Proteomics Bioinf.* **2015**, *13*, 17–24.
- (15) Villarroya-Beltri, C.; Gutiérrez-Vázquez, C.; Sánchez-Cabo, F.; Pérez-Hernández, D.; Vázquez, J.; Martín-Cofreces, N.; Martínez-Herrera, D. J.; Pascual-Montano, A.; Mittelbrunn, M.; Sánchez-Madrid, F. Sumoylated hnRNP A2/B1 Controls the Sorting of MiRNAs into Exosomes through Binding to Specific Motifs. *Nat. Commun.* **2013**, *4*, 2980.
- (16) Barker, J. N.; Mitra, R. S.; Griffiths, C. E.; Dixit, V. M.; Nickoloff, B. J. Keratinocytes as Initiators of Inflammation. *Lancet* **1991**, *337*, 211–4.
- (17) Pastore, S.; Mascia, F.; Mariani, V.; Girolomoni, G. Keratinocytes in Skin Inflammation. *Expert Rev. Dermatol.* **2006**, *1*, 279–291.
- (18) Miodovnik, M.; Koren, R.; Ziv, E.; Ravid, A. The Inflammatory Response of Keratinocytes and its Modulation by Vitamin D: The Role of MAPK Signaling Pathways. *J. Cell. Physiol.* **2012**, *227*, 2175–83.
- (19) Sinha, M.; Sen, C. K.; Singh, K.; Das, A.; Ghatak, S.; Rhea, B.; Blackstone, B.; Powell, H. M.; Khanna, S.; Roy, S. Direct Conversion of Injury-Site Myeloid Cells to Fibroblast-Like Cells of Granulation Tissue. *Nat. Commun.* **2018**, *9*, 936.
- (20) Lucas, T.; Waisman, A.; Ranjan, R.; Roes, J.; Krieg, T.; Muller, W.; Roers, A.; Eming, S. A. Differential Roles of Macrophages in Diverse Phases of Skin Repair. *J. Immunol.* **2010**, *184*, 3964–77.
- (21) Das, A.; Ganesh, K.; Khanna, S.; Sen, C. K.; Roy, S. Engulfment of Apoptotic Cells by Macrophages: A Role of MicroRNA-21 in the Resolution of Wound Inflammation. *J. Immunol.* **2014**, *192*, 1120–9.
- (22) Das, A.; Ghatak, S.; Sinha, M.; Chaffee, S.; Ahmed, N. S.; Parinandi, N. L.; Wohleb, E. S.; Sheridan, J. F.; Sen, C. K.; Roy, S. Correction of MFG-E8 Resolves Inflammation and Promotes Cutaneous Wound Healing in Diabetes. *J. Immunol.* **2016**, *196*, 5089–100.
- (23) Das, A.; Sinha, M.; Datta, S.; Abas, M.; Chaffee, S.; Sen, C. K.; Roy, S. Monocyte and Macrophage Plasticity in Tissue Repair and Regeneration. *Am. J. Pathol.* **2015**, *185*, 2596–2606.
- (24) Kim, D. K.; Lee, J.; Kim, S. R.; Choi, D. S.; Yoon, Y. J.; Kim, J. H.; Go, G.; Nhung, D.; Hong, K.; Jang, S. C.; Kim, S. H.; Park, K. S.; Kim, O. Y.; Park, H. T.; Seo, J. H.; Aikawa, E.; Baj-Krzyworzeka, M.; van Balkom, B. W.; Belting, M.; Blanc, L.; et al. EVpedia: A Community Web Portal for Extracellular Vesicles Research. *Bioinformatics* **2015**, *31*, 933–9.
- (25) Keerthikumar, S.; Chisanga, D.; Ariyaratne, D.; Al Saffar, H.; Anand, S.; Zhao, K.; Samuel, M.; Pathan, M.; Jois, M.; Chilamkurti, N.; Gangoda, L.; Mathivanan, S. ExoCarta: A Web-Based Compendium of Exosomal Cargo. *J. Mol. Biol.* **2016**, *428*, 688–692.
- (26) Andreu, Z.; Yáñez-Mó, M. Tetraspanins in Extracellular Vesicle Formation and Function. *Front. Immunol.* **2014**, *5*, 442–442.
- (27) Van Deun, J.; Mestdagh, P.; Agostinis, P.; Akay, O.; Anand, S.; Anckaert, J.; Martinez, Z. A.; Baetens, T.; Beghein, E.; Bertier, L.; Berx, G.; Boere, J.; Boukouris, S.; Bremer, M.; Buschmann, D.; Byrd, J. B.; Casert, C.; Cheng, L.; Cmoch, A.; Daveloose, D.; et al. EV-TRACK: Transparent Reporting and Centralizing Knowledge in Extracellular Vesicle Research. *Nat. Methods* **2017**, *14*, 228–232.
- (28) Van Deun, J.; Hendrix, A.; consortium, E.-T. Is Your Article EV-TRACKed? *J. Extracell. Vesicles* **2017**, *6*, 1379835.
- (29) Hu, P.; Yang, Q.; Wang, Q.; Shi, C.; Wang, D.; Armato, U.; Prà, I. D.; Chiarini, A. Mesenchymal Stromal Cells-Exosomes: A Promising Cell-Free Therapeutic Tool For Wound Healing and Cutaneous Regeneration. *Burns Trauma.* **2019**, *7*, s41038-019-0178-8.
- (30) He, X.; Dong, Z.; Cao, Y.; Wang, H.; Liu, S.; Liao, L.; Jin, Y.; Yuan, L.; Li, B. MSC-Derived Exosome Promotes M2 Polarization and Enhances Cutaneous Wound Healing. *Stem Cells Int.* **2019**, *2019*, 7132708.
- (31) Gallego-Perez, D.; Pal, D.; Ghatak, S.; Malkoc, V.; Higuera-Castro, N.; Gnyawali, S.; Chang, L.; Liao, W. C.; Shi, J.; Sinha, M.; Singh, K.; Steen, E.; Sunyecz, A.; Stewart, R.; Moore, J.; Ziebro, T.; Northcutt, R. G.; Homsy, M.; Bertani, P.; Lu, W.; et al. Topical Tissue Nano-Transfection Mediates Non-Viral Stroma Reprogramming and Rescue. *Nat. Nanotechnol.* **2017**, *12*, 974–979.
- (32) Guasconi, L.; Serradell, M. C.; Garro, A. P.; Iacobelli, L.; Masih, D. T. C-Type Lectins on Macrophages Participate in the Immunomodulatory Response to Fasciola Hepatica Products. *Immunology* **2011**, *133*, 386–396.
- (33) Drickamer, K. Engineering Galactose-Binding Activity into a C-Type Mannose-Binding Protein. *Nature* **1992**, *360*, 183–6.
- (34) Martínez-Pomares, L.; Linehan, S. A.; Taylor, P. R.; Gordon, S. Binding Properties of the Mannose Receptor. *Immunobiology* **2001**, *204*, 527–35.
- (35) Song, W.; Zhou, X.; Benktander, J. D.; Gaunitz, S.; Zou, G.; Wang, Z.; Novotny, M. V.; Jacobson, S. C. In-Depth Compositional and Structural Characterization of N-Glycans Derived from Human Urinary Exosomes. *Anal. Chem.* **2019**, *91*, 13528–13537.
- (36) Snyder, C. M.; Zhou, X.; Karty, J. A.; Fonslow, B. R.; Novotny, M. V.; Jacobson, S. C. Capillary Electrophoresis-Mass Spectrometry for Direct Structural Identification of Serum N-Glycans. *J. Chromatogr. A* **2017**, *1523*, 127–139.
- (37) Clerc, F.; Reiding, K. R.; Jansen, B. C.; Kammeijer, G. S.; Bondt, A.; Wührer, M. Human Plasma Protein N-Glycosylation. *Glycoconjugate J.* **2016**, *33*, 309–43.
- (38) Brancato, S. K.; Albina, J. E. Wound Macrophages as Key Regulators of Repair: Origin, Phenotype, and Function. *Am. J. Pathol.* **2011**, *178*, 19–25.

- (39) Mirza, R. E.; Koh, T. J. Contributions of Cell Subsets to Cytokine Production During Normal and Impaired Wound Healing. *Cytokine+* **2015**, *71*, 409–412.
- (40) Murray, P. J.; Allen, J. E.; Biswas, S. K.; Fisher, E. A.; Gilroy, D. W.; Goerdt, S.; Gordon, S.; Hamilton, J. A.; Ivashkiv, L. B.; Lawrence, T.; Locati, M.; Mantovani, A.; Martinez, F. O.; Mege, J.-L.; Mosser, D. M.; Natoli, G.; Saeij, J. P.; Schultze, J. L.; Shirey, K. A.; Sica, A.; et al. Macrophage Activation and Polarization: Nomenclature and Experimental Guidelines. *Immunity* **2014**, *41*, 14–20.
- (41) El Masry, M. S.; Chaffee, S.; Das Ghatak, P.; Mathew-Steiner, S. S.; Das, A.; Higueta-Castro, N.; Roy, S.; Anani, R. A.; Sen, C. K. Stabilized Collagen Matrix Dressing Improves Wound Macrophage Function and Epithelialization. *FASEB J.* **2019**, *33*, 2144–2155.
- (42) Mosser, D. M.; Edwards, J. P. Exploring the Full Spectrum of Macrophage Activation. *Nat. Rev. Immunol.* **2008**, *8*, 958–969.
- (43) Li, J.; Ghatak, S.; El Masry, M. S.; Das, A.; Liu, Y.; Roy, S.; Lee, R. J.; Sen, C. K. Topical Lyophilized Targeted Lipid Nanoparticles in the Restoration of Skin Barrier Function Following Burn Wound. *Mol. Ther.* **2018**, *26*, 2178–2188.
- (44) Kulkarni, J.; Cullis, P.; van der Meel, R. Lipid Nanoparticles Enabling Gene Therapies: From Concepts to Clinical Utility. *Nucleic Acid Ther.* **2018**, *28*, 146–157.
- (45) Rietwyk, S.; Peer, D. Next-Generation Lipids in RNA Interference Therapeutics. *ACS Nano* **2017**, *11*, 7572–7586.
- (46) Jayaraman, M.; Ansell, S. M.; Mui, B. L.; Tam, Y. K.; Chen, J.; Du, X.; Butler, D.; Eltepu, L.; Matsuda, S.; Narayanannair, J. K. Maximizing the Potency of siRNA Lipid Nanoparticles for Hepatic Gene Silencing. *Angew. Chem., Int. Ed.* **2012**, *51*, 8529–8533.
- (47) Barki, K. G.; Das, A.; Dixith, S.; Ghatak, P. D.; Mathew-Steiner, S.; Schwab, E.; Khanna, S.; Wozniak, D. J.; Roy, S.; Sen, C. K. Electric Field Based Dressing Disrupts Mixed-Species Bacterial Biofilm Infection and Restores Functional Wound Healing. *Ann. Surg.* **2019**, *269*, 756–766.
- (48) Roy, S.; Elgharably, H.; Sinha, M.; Ganesh, K.; Chaney, S.; Mann, E.; Miller, C.; Khanna, S.; Bergdall, V. K.; Powell, H. M.; Cook, C. H.; Gordillo, G. M.; Wozniak, D. J.; Sen, C. K. Mixed-Species Biofilm Compromises Wound Healing by Disrupting Epidermal Barrier Function. *J. Pathol.* **2014**, *233*, 331–343.
- (49) Ghatak, S.; Chan, Y. C.; Khanna, S.; Banerjee, J.; Weist, J.; Roy, S.; Sen, C. K. Barrier Function of the Repaired Skin Is Disrupted Following Arrest of Dicer in Keratinocytes. *Mol. Ther.* **2015**, *23*, 1201–10.
- (50) Nithya, S.; Radhika, T.; Jeddy, N. Loricrin - An Overview. *J. Oral Maxillofac. Pathol.* **2015**, *19*, 64–68.
- (51) Kalinin, A.; Marekov, L. N.; Steinert, P. M. Assembly of the Epidermal Cornified Cell Envelope. *J. Cell Sci.* **2001**, *114*, 3069–3070.
- (52) Sen, C. K.; Khanna, S.; Babior, B. M.; Hunt, T. K.; Ellison, E. C.; Roy, S. Oxidant-Induced Vascular Endothelial Growth Factor Expression in Human Keratinocytes and Cutaneous Wound Healing. *J. Biol. Chem.* **2002**, *277*, 33284–90.
- (53) Chan, Y. C.; Khanna, S.; Roy, S.; Sen, C. K. miR-200b Targets Ets-1 and Is Down-Regulated by Hypoxia to Induce Angiogenic Response of Endothelial Cells. *J. Biol. Chem.* **2011**, *286*, 2047–2056.
- (54) Das, A.; Abas, M.; Biswas, N.; Banerjee, P.; Ghosh, N.; Rawat, A.; Khanna, S.; Roy, S.; Sen, C. K. A Modified Collagen Dressing Induces Transition of Inflammatory to Reparative Phenotype of Wound Macrophages. *Sci. Rep.* **2019**, *9*, 14293.
- (55) Ganesh, K.; Das, A.; Dickerson, R.; Khanna, S.; Parinandi, N. L.; Gordillo, G. M.; Sen, C. K.; Roy, S. Prostaglandin E(2) Induces Oncostatin M Expression in Human Chronic Wound Macrophages through Axl Receptor Tyrosine Kinase Pathway. *J. Immunol.* **2012**, *189*, 2563–73.
- (56) Khanna, S.; Biswas, S.; Shang, Y.; Collard, E.; Azad, A.; Kauh, C.; Bhasker, V.; Gordillo, G. M.; Sen, C. K.; Roy, S. Macrophage Dysfunction Impairs Resolution of Inflammation in the Wounds of Diabetic Mice. *PLoS One* **2010**, *5*, e9539.
- (57) Garg, S.; Tang, J.; Rühle, J.; Naumann, C. Actin-Induced Perturbation of PS Lipid-Cholesterol Interaction: A Possible Mechanism of Cytoskeleton-Based Regulation of Membrane Organization. *J. Struct. Biol.* **2009**, *168*, 11–20.
- (58) Rhoades, E.; Ramlall, T. F.; Webb, W. W.; Eliezer, D. Quantification of  $\alpha$ -Synuclein Binding to Lipid Vesicles Using Fluorescence Correlation Spectroscopy. *Biophys. J.* **2006**, *90*, 4692–4700.
- (59) Gijsbers, A.; Nishigaki, T.; Sánchez-Puig, N. Fluorescence Anisotropy as a Tool to Study Protein-Protein Interactions. *J. Visualized Exp.* **2016**, No. 116, e54640.
- (60) Alley, W. R.; Novotny, M. V. Glycomic Analysis of Sialic Acid Linkages in Glycans Derived from Blood Serum Glycoproteins. *J. Proteome Res.* **2010**, *9*, 3062–3072.
- (61) Mitra, I.; Snyder, C. M.; Zhou, X.; Campos, M. I.; Alley, W. R.; Novotny, M. V.; Jacobson, S. C. Structural Characterization of Serum N-Glycans by Methylamidation, Fluorescent Labeling, and Analysis by Microchip Electrophoresis. *Anal. Chem.* **2016**, *88*, 8965–8971.
- (62) Riccardi, C.; Nicoletti, I. Analysis of Apoptosis by Propidium Iodide Staining and Flow Cytometry. *Nat. Protoc.* **2006**, *1*, 1458–1461.
- (63) Khanna, S.; Rink, C.; Ghoorkhanian, R.; Gnyawali, S.; Heigel, M.; Wijesinghe, D. S.; Chalfant, C. E.; Chan, Y. C.; Banerjee, J.; Huang, Y.; Roy, S.; Sen, C. K. Loss of miR-29b Following Acute Ischemic Stroke Contributes to Neural Cell Death and Infarct Size. *J. Cereb. Blood Flow Metab.* **2013**, *33*, 1197–206.
- (64) Rink, C.; Gnyawali, S.; Stewart, R.; Teplitsky, S.; Harris, H.; Roy, S.; Sen, C. K.; Khanna, S. Glutamate Oxaloacetate Transaminase Enables Anaplerotic Refilling of TCA Cycle Intermediates in Stroke-Affected Brain. *FASEB J.* **2017**, *31*, 1709–1718.
- (65) Somogyi, A.; Thissen, R.; Orthous-Daunay, F. R.; Vuitton, V. The Role of Ultrahigh Resolution Fourier Transform Mass Spectrometry (FT-MS) in Astrobiology-Related Research: Analysis of Meteorites and Tholins. *Int. J. Mol. Sci.* **2016**, *17*, 439.
- (66) Wu, Y.; Chen, L.; Scott, P. G.; Tredget, E. E. Mesenchymal Stem Cells Enhance Wound Healing through Differentiation and Angiogenesis. *Stem Cells* **2007**, *25*, 2648–59.
- (67) Chen, L.; Tredget, E. E.; Wu, P. Y.; Wu, Y. Paracrine Factors of Mesenchymal Stem Cells Recruit Macrophages and Endothelial Lineage Cells and Enhance Wound Healing. *PLoS One* **2008**, *3*, e1886.
- (68) Chen, L.; Tredget, E. E.; Liu, C.; Wu, Y. Analysis of Allogenicity of Mesenchymal Stem Cells in Engraftment and Wound Healing in Mice. *PLoS One* **2009**, *4*, e7119.
- (69) Ghatak, S.; Li, J.; Chan, Y. C.; Gnyawali, S. C.; Steen, E.; Yung, B. C.; Khanna, S.; Roy, S.; Lee, R. J.; Sen, C. K. AntihypoxamiR Functionalized Gramicidin Lipid Nanoparticles Rescue against Ischemic Memory Improving Cutaneous Wound Healing. *Nanomedicine* **2016**, *12*, 1827–1831.
- (70) Deng, B.; Ghatak, S.; Sarkar, S.; Singh, K.; Das Ghatak, P.; Mathew-Steiner, S. S.; Roy, S.; Khanna, S.; Wozniak, D. J.; McComb, D. W.; Sen, C. K. Novel Bacterial Diversity and Fragmented eDNA Identified in Hyperbiofilm-Forming *Pseudomonas aeruginosa* Rugose Small Colony Variant. *iScience*. **2020**, *23*, 100827.
- (71) Ahmed, N. S.; Ghatak, S.; El Masry, M. S.; Gnyawali, S. C.; Roy, S.; Amer, M.; Everts, H.; Sen, C. K.; Khanna, S. Epidermal E-Cadherin Dependent Beta-Catenin Pathway Is Phytochemical Inducible and Accelerates Anagen Hair Cycling. *Mol. Ther.* **2017**, *25*, 2502–2512.
- (72) Schindelin, J.; Arganda-Carreras, I.; Frise, E.; Kaynig, V.; Longair, M.; Pietzsch, T.; Preibisch, S.; Rueden, C.; Saalfeld, S.; Schmid, B.; Tinevez, J.-Y.; White, D. J.; Hartenstein, V.; Eliceiri, K.; Tomancak, P.; Cardona, A. Fiji: An Open-Source Platform for Biological-image Analysis. *Nat. Methods* **2012**, *9*, 676–682.
- (73) Bolte, S.; Cordelieres, F. P. A Guided Tour into Subcellular Colocalization Analysis in Light Microscopy. *J. Microsc.* **2006**, *224*, 213–32.